

Factors influencing the stability of natural gas foam prepared by alkyl polyglycosides and its decay rules

Yiping Wen^{a,b}, Nanjun Lai^{a,b,*}, Wenhong Li^{b,c}, Yongqiang Zhang^{b,c}, Zhaofeng Du^{b,c}, Lijuan Han^{a,b}, Zhiling Song^{a,b}

^a School of Chemistry and Chemical Engineering, Southwest Petroleum University, Chengdu, 610500, People's Republic of China

^b State Engineering Laboratory of Low-permeability Oil & Gas Reservoir Exploration and Development, Xi'an, 710018, People's Republic of China

^c Exploration and Development Research Institute of Changqing Oilfield, PetroChina, Xi'an, 710018, People's Republic of China



ARTICLE INFO

Keywords:
Alkyl polyglycosides
Natural gas foam
Drainage kinetics
Decay rules
Statistics methods
Surface properties

ABSTRACT

By using alkyl polyglycoside (APG) as foaming agent and natural gas as gas phase, the natural gas foam system was prepared, and the influence of alkyl chain length, metal cation valence and concentration, and polymer types on the foam stability was studied. By completely observing the volume and time required for the foam drainage liquid under different conditions, a foam drainage kinetics model was established. The drainage rate constant, the maximum drainage rate and its occurrence time during the foam drainage process can be acquired by derivation of the fitting function. The *Arrhenius* equation was adopted to fit the drainage rate constant at different temperature, and the drainage activation energy is obtained. The drainage process of foam was further analyzed from the perspective of kinetics. Moreover, the changes in geometric geometrics such as bubble number, particle size distribution frequency and the average diameter of the bubble in the decay process under different conditions was counted. According to the mathematical relationship between the average diameter and time, the *Ostwald* ripening rate and gas molecule diffusion constant are calculated. Finally, through the investigation of the interface properties and the micromorphology of the solution, the reasons for the above rules are explained. The research shows that: 1) the increase of the alkyl chain length of APG within a certain range (8–10.9) is beneficial to the improvement of the foam stability, and the continuous increase of chain length (10.9–12) is adverse to the foam stability, 2) the increase in the salinity of prepared water and the metal ions valence enhances the foam stability to a certain extent, 3) DG is more stable to APG foam than XG and KYPAM-6s. This study enriches the stability rules of APG foam with natural gas as the gas phase under different conditions, and provides ideas and methods for quantitatively analyzing the foam decay process from the perspectives of kinetics and statistics, which provides theoretical support for the application of natural gas foam in enhance oil recovery.

1. Introduction

Foam is an oil displacement system that successfully controls fluid mobility control in a reservoir (Pei et al., 2010; Xu et al., 2015). Foam flooding has been exploratory tested in oilfields since the 1960s. Theoretical tests and field practice have established the importance of foam fluid as an oil displacement system, and its application scope has been greatly expanded to drilling, flooding, fracturing and acidification, and other aspects of oilfield development (Kuru et al., 2005; Stewart et al., 2015; Parlar et al., 1995; Rossen et al., 1999; Kam et al., 2007). With its fluid properties, foam shows potential to be a smart fluid in oilfield (Weaire et al., 2008; Farajzadeh et al., 2007; Liu et al., 2006; Kovscek

et al., 2002; Vassenden et al., 1998; Chang et al., 1998; Garrett et al., 2006; Nguyen et al., 2005; Paulson et al., 1996). Its high apparent viscosity can control the displacement phase mobility and improve its sweep scope. The foaming agent reduces oil–water interfacial tension and can continue to play its role as a surfactant after the foam is defoamed. In addition to its control of displacement fluid mobility, foam can trap a large amount of gas and effectively supplement the formation energy. Foam system composed of different gases and foaming agents have various effects in the reservoir. Selecting an appropriate foam systems according to reservoir conditions can improve the effect of enhanced oil recovery (EOR) of foam flooding.

Classifies foam by gas phase type, currently, foam systems commonly

* Corresponding author. School of Chemistry and Chemical Engineering, Southwest Petroleum University, Chengdu, 610500, People's Republic of China.
E-mail address: lainanjun@swpu.edu.cn (N. Lai).

used in the oilfield development industry includes: air foam (Lang et al., 2019; Dong et al., 2012), N₂ foam (Sun et al., 2016; Pang et al., 2015; Liang et al., 2019; Hurtado et al., 2020), CO₂ foam (Xu et al., 2017; Yang et al., 2019; Zhang et al., 2020; Du et al., 2016) and natural gas foam (Xu et al., 2018; Salman et al., 2019). Local reservoir conditions (especially physical and chemical properties of crude oil), downhole strings, and local gas source considered when selecting the type of gas phase during site construction. However, before applying the foam system, the foam stability under reservoir conditions needs to be researched. In recent years, the foam stability investigation has not been limited to the measurement of half-life of drainage liquid and foam, researchers hope to quantitatively describe the overall process of foam decay. Lioumbas et al. (2015) used microscope to observe the bubble coarsening process, and quantitatively described the coarsening process of bubble particle size with the Leonard-Lemlich drainage kinetic model. Based on the fractal theory, Wang et al. (2017) used fractal dimension to study the dynamic structure of foam in porous medium, the study found that fractal dimension has time dependence and can better describe the foam decay process. Zhu (2019a) used microscope to record the foam decay process, counted geometric information such as average particle size and ellipticity during the decay process, and according to the mathematical relationship between the average particle size and time, the Ostwald ripening rate of the bubble in decay process is obtained. Based on this method, Zhu (2019b) used the box-counting method to calculate the fractal dimension of the foam decay process, and adopt fractal dimension to measure the irregularity in the foam decay process. Moreover, the polydispersity coefficient U_{poly} and the gas mass transfer rate are calculated according to the change of particle size change, these analysis methods are helpful to quantitatively describe the coarsening process of foam.

APG is a new type of efficient environmental-friendly foaming agent prepared through glucose and fatty alcohol dehydration and has been widely used in detergents, cosmetics, pharmaceuticals and other industries. Only a few reports were available on APG application in oilfield chemistry. The biopolysaccharide APG has a good tolerance to temperature and salinity. Compared with other types of surfactants, this substance has good EOR ability in core flooding experiments (Iglauer et al., 2009; Yin et al., 2013; Wei et al., 2018, 2020; Rafati et al., 2012). The commonly used foaming agents (SDBS or AOS) cannot adapt to harsh reservoir conditions, whereas APG is largely independent of temperature and salinity and thus shows promise as a foaming agent. The natural gas in the natural gas foam interacts with the crude oil in the reservoir. During defoaming, the internal gas phase partially dissolves in the crude oil, thus reducing the viscosity of the crude oil and improving the mobility ratio of the displacement phase to the displaced phase. Moreover, the hydrophobic components of water-based foaming agent are similar to those of natural gas, making the latter easier to foam compared with other gases. Therefore, introducing natural gas into APG aqueous solution to form natural gas foam can achieve an enhanced recovery effect. Compared with those of other gas-types foams, the properties of natural gas foams are rarely reported. Other properties (foam drainage kinetics, coarsening behavior) must be further studied prior to the application of natural gas foam to improve oil recovery.

This study aims introduce chemical reaction kinetics into the study of the kinetics of the physical process of foam drainage. The factors influencing the drainage kinetics of natural gas foam system prepared by APG were investigated to explore the effects of alkyl chain length of APG, inorganic salts in different valence states (including different salinities) and different types of polymers (including different concentrations) on the drainage kinetics of natural gas foam. In addition, statistical methods (Zhu et al. 2019a, 2019b) were used to study the decay of natural gas foam system prepared by APG under different conditions and the influence trend of the above factors on the coarsening behavior of bubble. The results will further clarify the decay mechanism of natural gas foam system and provide theoretical support for natural gas foam application in EOR.

2. Experimental

2.1. Materials and instruments

2.1.1. Materials

- (1) Foaming agents: APG-08, APG-0810, APG-10, APG-0814, APG-12, the effective content of the all five APGs used in this study is 50%. The average alkyl chain length are shown in Table 1.
- (2) Inorganic salts: NaCl, CaCl₂, chemically pure.
- (3) gas: natural gas, the methane content is 99%.
- (4) polymers: xanthan gum (XG), purity 99%, molecular weight 2.0×10^6 g/mol, diutan gum (DG), purity 99%, molecular weight 5.2×10^6 g/mol.

KYPAM-6s, purity 88.87%, hydrolyzing degree 26.30%, molecular weight 8.0×10^6 g/mol.

The above three polymers are dry powders, and their molecular formulas are shown in Fig. 1.

2.1.2. Instruments

- a. Foam performance evaluation instrument, fabricate by the authors, the physical picture and the specific parameter are shown in Supplementary Materials (Section 1).
- b. The monitoring unit of foam performance evaluation instrument: FDR-AX700 camera, mainly used to monitor the drainage volume of foam system with time.
- c. Visual observation model: fabricate by the authors, see the Supplementary Materials (Section 2) for the physical model and specific parameter.
- d. Microscopic observation unit: BS-200SS microscope, see the Supplementary Materials (Section 3) for the specific parameter.
- e. Other instruments: TX-500C rotary droplet interface tensiometer, FEI Quanta 450 environmental scanning electron microscope (ESEM).

2.2. Preparation of natural gas foam system

The preparation steps of the natural gas foam system are shown in Supplementary Materials (Section 4).

2.3. Measurement of natural gas foam drainage

When the mixer is turned on for 2 min, turn off the mixer power, record the foam height h_1 , and turn on the camera to record the foam drainage until the height of the drainage liquid is close to or equal to h_0 . If the height of the liquid level remained unchanged even after 1 h, the experiment of this group ends. Record the change over time of the rising height of the drainage interface in the foam evaluation instrument and convert it to volume over time and mean value method has been used to minimized error. In this paper, we studied the drainage kinetics of APG under different alkyl chain lengths, different types of inorganic salts (including different salinities) and different types of polymers (including different concentrations). The experimental arrangement is as follows:

- (1) Natural gas foam drainage kinetics of different alkyl chain length of APG: foaming agents APG-08, APG-0810, APG-10, APG-0814 and APG-12, the concentration of each APG are all 6 g/L with distilled water, and the effect of alkyl chain length on the drainage kinetics of natural gas foam was mainly researched.
- (2) Effect of inorganic salts on the drainage kinetics of natural gas foam: The concentration of foaming agent APG-10 was 6 g/L, and the salinity of prepared brine is 20 g/L, 40 g/L, 60 g/L, 80 g/L and 100 g/L. NaCl and CaCl₂ were selected to prepare the brine at the corresponding salinity. The effects of cation valence (Na⁺ and

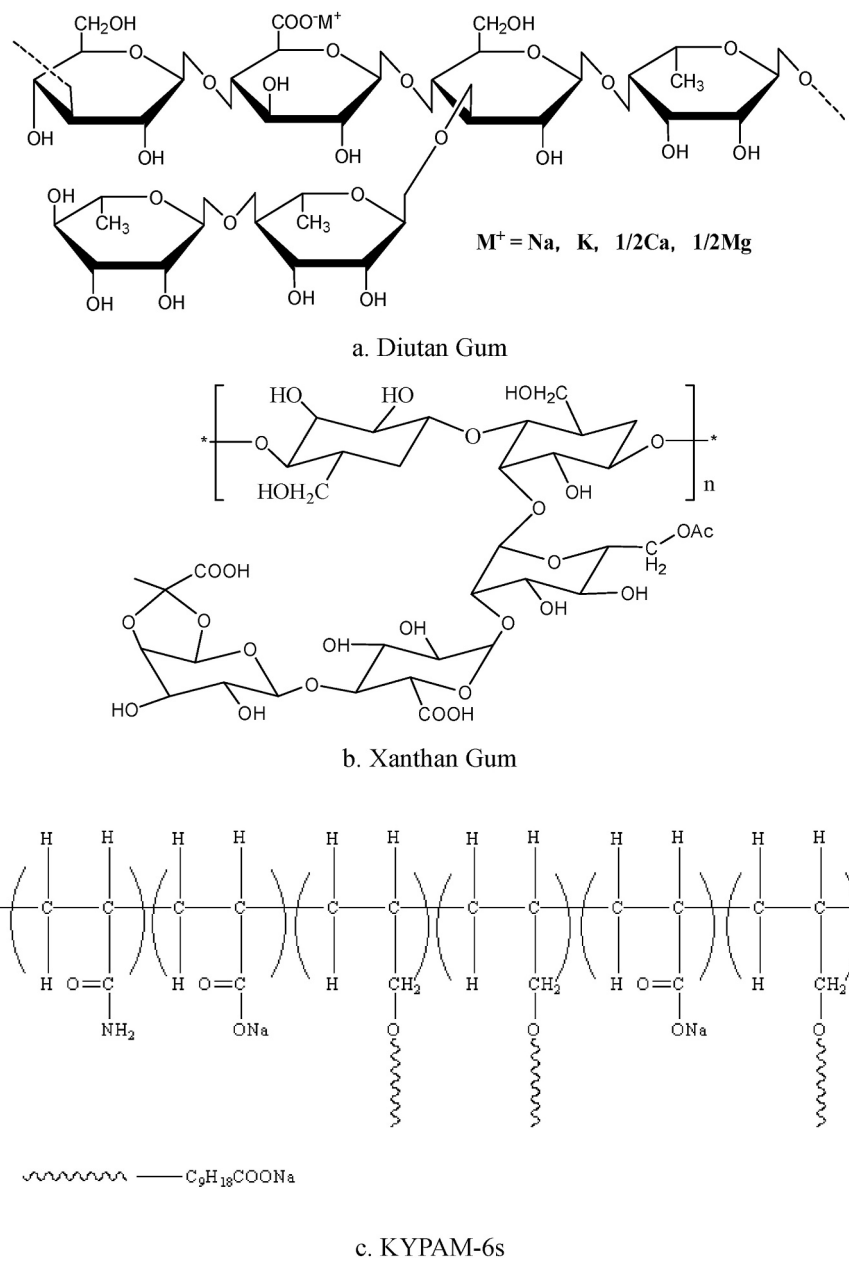


Fig. 1. Molecular formulas of three polymers.

Ca^{2+}) and salinity on the drainage kinetics of natural gas foam were mainly studied.

- (3) Effects of polymers on the drainage kinetics of natural gas foam: The concentration of foaming agent APG-10 is 6 g/L, and the polymer concentration in the prepared water all 0.10 g/L, 0.25 g/L, 0.50 g/L and 0.75 g/L. The target concentration of DG, XG and KYPAM-6s were added to the foaming agent aqueous solution to explore the effect of polymer types on the drainage kinetics of natural gas foam.

After drawing the relationship curves between drainage volume and time of natural gas foam system, the drainage process of natural gas foam can be fitting with some form of function, then the drainage kinetics equation and the drainage rate constant k_d under corresponding conditions can be obtained. In order to obtain the activation energy of natural gas foam under each condition, we studied the drainage of the foam under different conditions at different temperatures, and the temperatures are 20 °C, 40 °C, 60 °C and 80 °C. After obtaining k_d at

different temperatures, *Arrhenius* equation was used to fit k_d at different temperatures ($k_d \sim T^{-1}$), and the activation energy E_a of drainage liquid under the corresponding conditions could be obtained. By comparing the E_a , we can acquire the energy barriers that natural gas foam needs to overcome during drainage under different conditions.

2.4. The behavior of natural gas foam coarsening

Connect the foam performance evaluation instrument to the heated observation model and adjust the microscope position. After high speed stirring for 2 min, quickly displace the foam into the model from both inlet and outlet valves by using the internal pressure of the foam performance evaluation instrument. After the inside of the observation model is filled with foam, close the inlet and outlet valves of the model, and set the S-EYE software equipped with the microscope to take pictures of the natural gas foam inside the model every 1 min. The experimental arrangement is the same as that in section 2.3. This article only explores the coarsening behavior of natural gas foam at 60 °C under

different conditions. The observation device for foam decay process is shown in Figure S2.

After obtaining the photos of natural gas foam at different times under different conditions, the Nanomeasure 1.2 software was used to measure the bubble diameter in the photos. The occurrence frequency of bubble diameter in a particle size range at a certain time was calculated and the particle size distribution (PSD) curve was drawn. Additionally,

we also made statistics on the bubble numbers at different times, and plotted the time-bubble number curves under different conditions.

The average diameter of the bubbles (D_{ad}) in a photo at a certain time can be calculated by equation (1), and the curve of time- D_{ad} can be drawn. In equation (1) (Zhu et al., 2019b), where D_i is the single bubble diameter, and n_b is the bubble numbers in the photo.

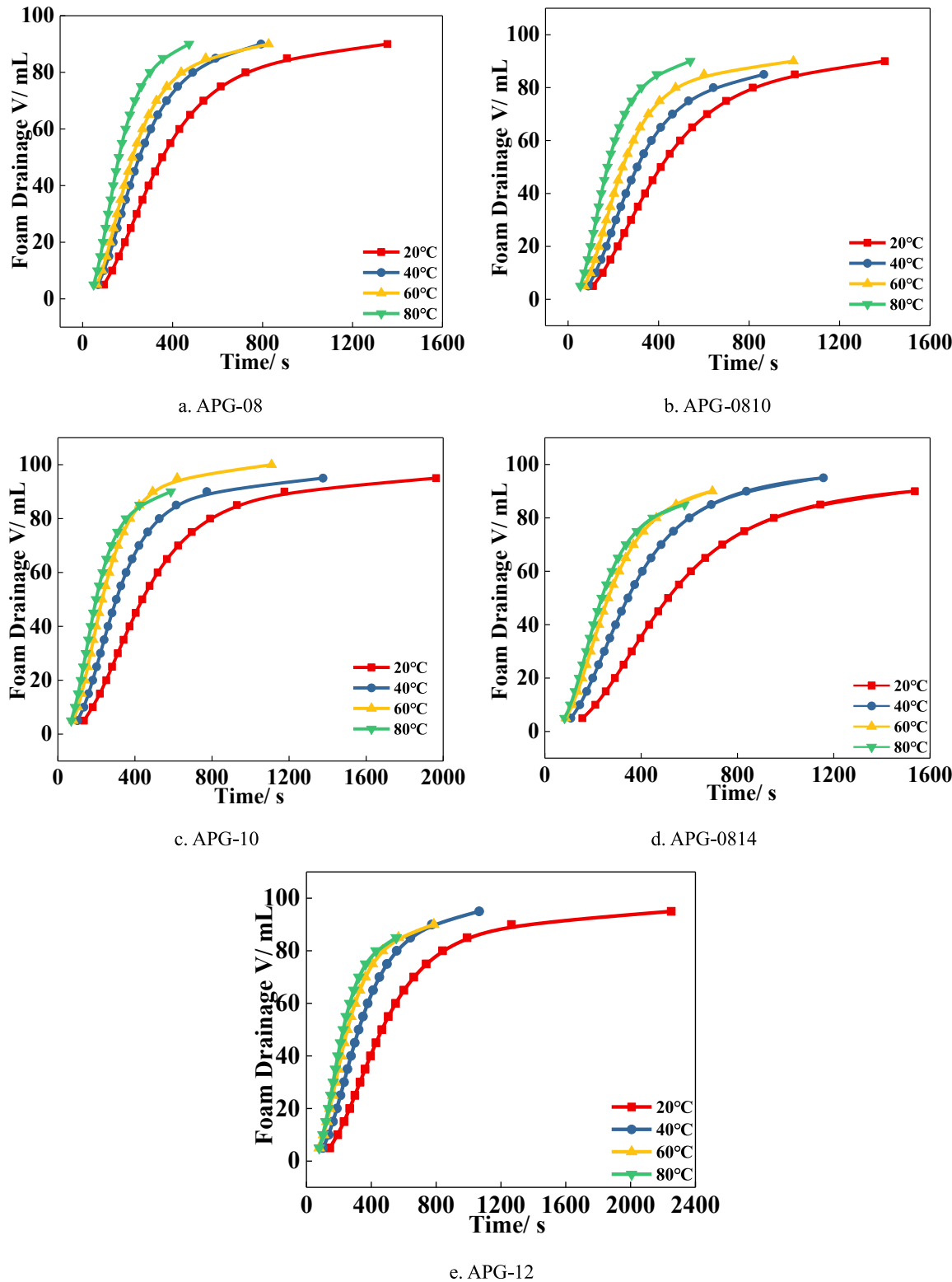


Fig. 2. The relation curves of drainage volume and time of APG with different alkyl chain lengths at different temperature.

$$D_{ad} = \frac{\sum_{i=1}^n D_i}{n_b} \quad (1)$$

The polydispersity coefficient U_{poly} of bubbles can be calculated by equation (2) (Schmitt et al., 2004), where \bar{D}^2 is the average value of the bubble diameter squared, \bar{D}^2 is the square of the average bubble diameter, \bar{D} is the average bubble diameter.

$$U_{poly} = \frac{\sqrt{\bar{D}^2 - \bar{D}^2}}{\bar{D}} \quad (2)$$

According to the calculation model proposed by Schmitt and Cattelet (2004), the Ostwald ripening rate of a colloidal system can be calculated under certain conditions, which is, the change of a certain thermodynamically unstable system with the pass of time. Ostwald ripening rate can be used to measure the relative stability of thermodynamically unstable systems such as foams and emulsions, the calculation formula is shown in equation (3) (Schmitt et al., 2004), where Ω is the Ostwald ripening rate, D_c is the critical diameter (equivalent to the D_{ad} in this article), γ is the gas-liquid interfacial tension, D_{diff} is the diffusion coefficient of natural gas molecules, S is the solubility of gas, F is the correction factor, and V_m is the molar volume of gas, R is the molar gas constant, T is the Kelvin temperature. By plotting the curve of time and cubic average diameter (D_{ad}^3) and linear fitting, the slope of the obtained line is the Ostwald ripening rate under certain conditions. The larger the value, the more unstable the foam system is.

$$\Omega = \frac{d(D_c)^3}{dt} = \frac{64\gamma D_{diff} S F V_m}{9RT} \quad (3)$$

2.5. Surface properties of APG aqueous solution

The surface tension measurement device (TX-500C rotary droplet interface tensiometer) and the gas-liquid surface tension measurement procedure of the natural gas – foaming agent solution are shown in Supplementary Materials (Section S5).

2.6. Micromorphology of bulk phase of foam system

FEI Quanta 450 ESEM is used to observe the micromorphology of the foam system bulk phase, see Supplementary Materials (Section S6) for the steps and related parameters adopted during the test.

3. Results and discussion

3.1. Decaying of APG foam with different alkyl chain lengths

3.1.1. Effect of alkyl chain length on the drainage kinetics of APG foam

The change in the drainage volume of natural gas foam systems prepared with APG-08, APG-0810, APG-10, APG-0814, and APG-12 at different temperatures over time is shown in Fig. 2. All the curves formed by the discrete data points basically have the same “L” shape, indicating that the natural gas foam prepared by APG with different alkyl chain length exhibit commonality in the drainage process and has a potential common law that is not affected by system composition and temperature.

Hill function (equation (4), Yan et al., 2005) was used to fit the above drainage curve to describe the drainage process of natural gas foam prepared by APG with different alkyl chain lengths in Fig. 2.

$$V_t = V_{max} \frac{t^n}{K^n + t^n} \quad (4)$$

where the t is drainage time (s); V_t is the drainage volume at time t (mL); V_{max} is the model parameter; that represents the maximum drainage of foam system (mL); K is the model parameter, and its physical meaning can be obtained from the data in Table 1; and n is the model parameter

that represents the inverse characteristic function of the drainage liquid volume–time curve. Data-processing software was used to fit the above discrete data points and obtain the values of the model parameters V_{max} , K and n . The correlation coefficients R^2 are all higher than 0.99, the fitting results of all curves are shown in Table 2.

Comparison of K with the time corresponding to the drainage volume revealed that K is the half-life during the drainage of the foam system. At different temperatures, the drainage half-life of natural gas foams prepared by APG first increases and then decreases with the average alkyl chain length in APG molecules. In this experiment, the short chain APG (e.g., APG-08) exhibits serious coalescence behavior after the foaming, leading to fast defoaming. However, the defoaming of other APGs with long alkyl chain length has a slow rate and is mainly based on bubble coarsening. The alkyl chain length in the APG molecules is directly related to the formation and stability of the foam. When the APG alkyl chain length is low, the foam system is unstable, when the chain length is long (e.g., APG-12), the stability of the foam system decreases. Only when the alkyl chain is moderate in length (such as APG-0810, APG-10 and APG-0814) that APG can form abundant foam with good stability. The changes of E_a and drainage rate of natural gas foam formed by APG and the effect of alkyl chain length on foam drainage were also studied.

The derivative of t in equation (4) was calculated to obtain the equation of natural gas foam drainage rate (equation (5)) can be obtained:

$$\frac{dV_t}{dt} = \frac{nV_{max} K^n t^{n-1}}{(K^n + t^n)^2} \quad (5)$$

Equation (4) was transformed to derive the expression for t (equation (6))

$$t = K \left(\frac{V_t}{V_{max} - V_t} \right)^{\frac{1}{n}} \quad (6)$$

Equation (7) can be obtained by substituting the expression of t into equation (5).

$$\frac{dV_t}{dt} = \left(\frac{n}{V_{max} K} \right) V_t^{\left(\frac{1-n}{n} \right)} (V_{max} - V_t)^{\left(\frac{1+n}{n} \right)} \quad (7)$$

In equation, $\frac{n}{V_{max} K}$ represents the specific rate constant of the drainage process. Therefore, the rate constant (k_d) in the drainage can be calculated by equation (8).

$$k_d = \frac{n}{V_{max} K} \quad (8)$$

Dimensional calculation from equation (8) shows that the physical dimension of the k_d is $(\text{mL}\cdot\text{s})^{-1}$. According to the assumption of the drainage model, the K can be calculated from the half-life time $t_{1/2}$ of drainage:

$$K = t_{1/2} \quad (9)$$

Assuming the k_d satisfies the Arrhenius equation (equation (10))

$$\ln k_d = \ln A - \frac{E_a}{RT} \quad (10)$$

In equation (10), A is the preexponential factor, E_a is the activation energy (J/mol), R is the gas molecular constant (8.314 J/K·mol), and T is

Table 1
Average carbon chain length.

Composition	Chain length	Molecular weight
APG-08	8	292
APG-0810	9	306
APG-10	10	320
APG-0814	10.9	334
APG-12	12	346

Table 2

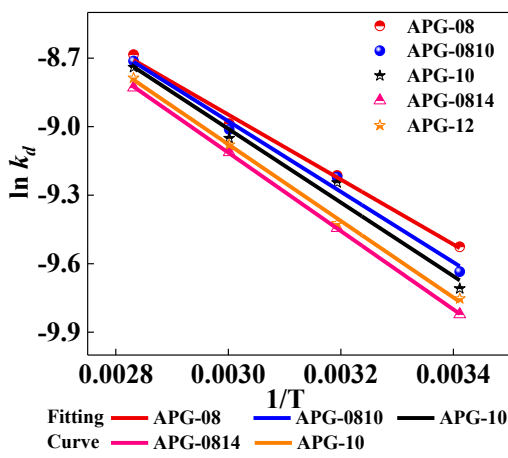
Fitting parameters of natural gas foam drainage curve of APG with different alkyl chain lengths.

Temperature/°C	Composition	V _{max}	K	n	R ²
20	APG-08	93.6917	333.8388	2.28	0.9981
	APG-0810	94.8850	390.0457	2.42	0.9901
	APG-10	97.0421	427.7978	2.52	0.9998
	APG-0814	95.0230	490.8427	2.54	0.9912
	APG-12	96.6135	452.5217	2.53	0.9926
	APG-08	95.8	242.0881	2.31	0.9930
40	APG-0810	90.0983	279.1155	2.487	0.9951
	APG-10	96.3859	295.0538	2.746	0.9993
	APG-0814	99.312	342.8358	2.543	0.9923
	APG-12	93.6483	320.6850	2.574	0.9964
	APG-08	93.1606	208.3759	2.43	0.9943
	APG-0810	93.894	220.2999	2.53	0.9976
60	APG-10	97.3333	237.5037	2.756	0.9911
	APG-0814	94.1944	255.044	2.687	0.9976
	APG-12	96.07	240.5904	2.591	0.9913
	APG-08	95.5355	155.0822	2.5	0.9987
	APG-0810	94.3347	166.0499	2.571	0.9914
	APG-10	93.6397	189.0974	2.8352	0.9900
80	APG-0814	90.1574	218.9783	2.88	0.9921
	APG-12	90.153	210.0815	2.891	0.9931

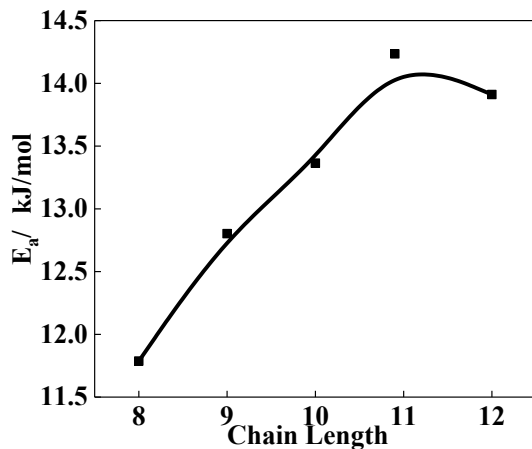
the Kelvin temperature (K). Equation (8) was used to calculate the data in Table 1, and obtain the k_d of APG with different alkyl chain lengths at various temperatures (293.15, 313.15, 333.15, and 353.15 K). $\ln k_d \sim T^{-1}$ was plotted and is shown in Fig. 3, and linear fitting was conducted on the data points. Fig. 3 shows good linear relationship between $\ln k_d$ and T^{-1} ($R^2 > 0.99$), which conforms to the Arrhenius equation. The absolute value of each fitted curve slope was multiplied by the gas molecular constant to obtain the drainage activation energy. When the alkyl chain length increases within a certain range (8 → 10.9), the E_a of foam drainage also increases from 11.787 kJ/mol to 14.235 kJ/mol. This finding indicates that with the increase in the alkyl chain, the E_a of foam drainage increases, and the large energy barrier must be overcome during drainage. When the alkyl chain length continues to grow (10.9 → 12), the E_a of drainage and the energy barrier decrease, but the drainage rate of foam increases.

The derivative of the drainage volume–time curve of the foam system was obtained, and the change of drainage rate of foam formed by APG with different alkyl chain lengths at the same temperature ($T = 60$ °C, Fig. 4) was analyzed. The curve shape of the derivative function is basically the same: at the initial drainage stage, the foam drainage rate increases rapidly until the inflection point of the drainage curve, at which time the corresponding liquid drainage rate reaches its maximum

value. The drainage rate then begins to decline until the end of the process and reaches the maximum drainage volume V_{max} . Jacobi et al. (1956) believed that the change law of drainage rate results from the rearrangement of the liquid in the foam column. In the initial state, the liquid in the foam column is evenly distributed and then rearranged to ensure that the liquid at the foam column bottom is thickened and at the maximum concentration. The drainage rate continuously increases under gravity. When the liquid distribution is rebalanced, the drainage rate reaches a maximum value and then gradually decreases until the rate approaches 0. Therefore, the drainage process can be divided into two stages. First is the initial stage, in which the liquid film is thick mainly due to gravity, and the drainage rate is fast. This stage is the main step in foam drainage, and completes most of the drainage volume (i.e., the control phase). Fig. 4 shows that during the control phase, with the growth of alkyl chain length (8 → 10.9), the extreme value of drainage rate gradually decrease, and the time when the extreme value appears gradually shifts to the right. This phenomenon occurs mainly due to the strong liquid film formed by long-chain APG molecules, which obstructs the gravity-induced drainage to some extent, resulting in prolonged overall drainage time of foam. The second stage is the drainage under the action of capillary force, which corresponds to the part of the drainage curve that is close to equilibrium. This stage is mainly the thinning of the foam liquid film (thinning stage). When the curvature radius of the foam film is smaller than the Plateau borders, the static pressure at the foam film is higher than that of the Plateau borders, causing the aqueous phase in the liquid film to continue to move toward this place (Xu et al., 2016). The drainage rate of the foam remains small until the liquid film becomes thin (<100 nm). Figure- 4b shows that when the alkyl chain length is within a certain range, the drainage rate gradually increases. Given that this stage is not a control stage, which means the drainage rate gradually increases but does not substantially affect the overall drainage time. At this stage, the van der Waals' force between the foam film plays a decisive role and continuously thins out the film. Finally, the liquid film ruptures, and the bubbles coalesce. This conclusion is consistent with the two-stage theory of Save et al. (1994). Given that this stage is controlled by capillary, the rate in this stage is positively correlated with capillary force. A great capillary force between bubbles indicates a fast rate in this stage. According to the Laplace equation, the gas–liquid interfacial tension is proportional to the capillary force between the bubbles. This stability law (the foam stability increases first and then decreases with the alkyl chain length of APG) will be discussed by studying the gas–liquid interface adsorption properties of APG with different alkyl chain lengths (see section 3.1.3).



a. fitted curves

b. change of E_a with alkyl chain lengthFig. 3. Arrhenius fitting curve (a) and E_a (b) of drainage process of foam formed by APG with different alkyl chain lengths.

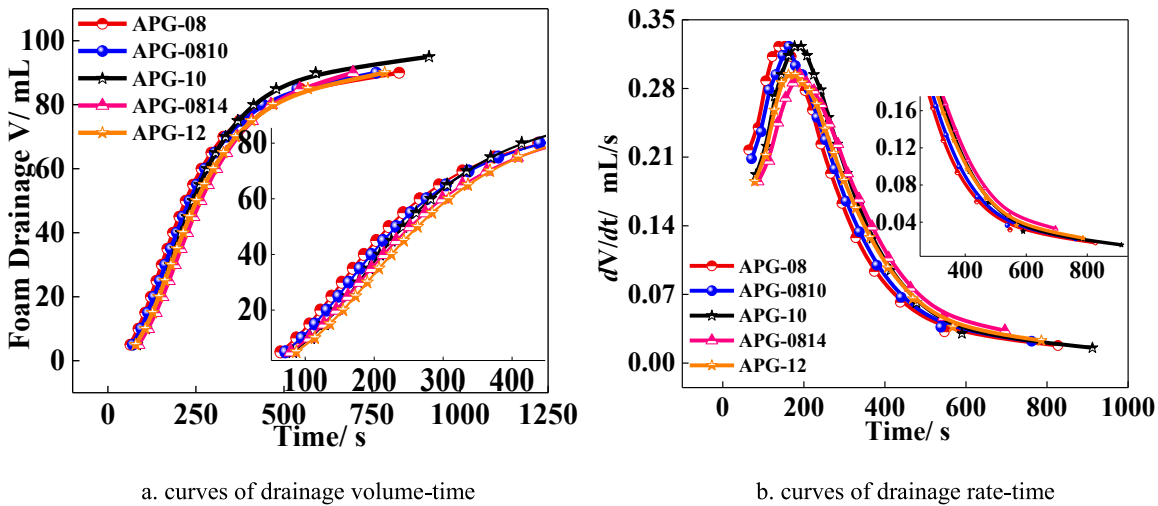


Fig. 4. The relationship between drainage volume and time (a) and the corresponding relationship drainage rate and time (b).

3.1.2. Coarsening of foam formed by APG with different alkyl chain lengths

After foam formation, gas diffusion occurs between the bubbles inside, that is, the coarsening behavior (Stubenrauch et al., 2017). During coarsening, the gas molecules diffuse from small bubbles to large bubbles. The bubbles with small curvature radius continue to become smaller until they disappear, and those with large radius of curvature continuously grow. The following characteristics of bubbles were analyzed to explore the behavior of foam coarsening: (1) changes in the bubble number in the visual field, (2) bubble diameter distribution, (3) mean bubble diameter, and (4) variation of U_{poly} . The effect of gravity drainage can be excluded because the morphological changes of 2D bubbles were recorded by a microscope in a specifically closed model. The evolution of foam under different conditions was studied quantitatively through the image analysis of foam photographs. The evolution of foam formed by APG-08, APG-0810, APG-10, APG-0814, and APG-12 within 0–30 min is shown in Fig. 5. Foam defoaming is mainly based on the coarsening behavior, and no bubble coalescence is observed. APG-08 (worst stability) and APG-0814 (best stability) were used as examples to plot the variation of bubble diameter distribution during foam decay (Fig. 6). After foaming, the bubble diameter distribution is relatively uniform within 15–160 μm under the initial conditions, and the main peak diameter is 60 μm . Bubble coarsening becomes evident with time as manifested by the decrease in bubble numbers (Figure- 7a) and the increase in the D_{ad} (Figure- 7b). Owing to the capillary force, the gas in the small bubbles gradually diffuses to the large bubbles, leading to the uneven distribution of bubble diameter. In addition, the distribution range of the main peak diameter decreases. The PSD curve evolves from the single-peak distribution in the initial stage to multi-peak distribution, and the bubble uniformity decreased. Fig. 6 also showed that the foam of APG-08 exhibits the most serious disproportionation at 30 min. The distribution range of foam diameter has expanded to 38–1100 μm , and a high frequency distribution (42.59%) is found in the 238–1100 μm . For APG-0814, the diameter range has only expanded to 20–450 μm , and the degree of bubble diameter disproportionation is relatively weak. The coarsening rate of foam formed by APG-08 is higher than that of APG-0814, and the bubbles are easily to coalesce and become enlarged.

Variations in the bubble numbers and D_{ad} of foam formed by APG with different alkyl chain length during decay are shown in Fig. 7. At the same temperature, the bubble number gradually decreases with time. However, the decline is not linear but shows an L-shaped curve. In the first 5 min, the bubble number decreases the fastest (compared with the overall trend). Within 5–10 min, the bubble number decreases slowly but still exhibits a large decline rate. After 10 min, the bubble number is

still decreasing, but the decreasing degree is linear and the decreasing speed is stable. Within a certain range, the decrease rate of the bubble number in the initial stage (0–5 min) gradually decreases when the length of chain of APG increases. Within the observation time (30 min), the bubble numbers is always higher than the APG with short chain length. This change corresponds to the D_{ad} change of bubbles at different times. For APG-08, the bubble diameter suddenly increases in the initial stage. In the first 5 min, the D_{ad} increases from 70 μm to 239.29 μm with an increase of 3.42 times. At 5–20 min, the growth rate of bubble diameter is significantly lower than that in the initial stage. After 20 min, the D_{ad} still increases, but the increase is not large from 365.02 μm to 392.54 μm . For APG-0814, the D_{ad} increases from 60.12 μm to 100.11 μm , with an increase of only 1.67 times, and the diameter shows a linear increase with time. During the observation time, the D_{ad} increases from 60.12 μm to 200 μm with an increase of only 3.33 times, and the foam decay process is slower than that of APG-08. Similar to section 3.1.1, foam stability slightly decreases when the average alkyl chain length of APG molecules continues to increase (10.9 → 12). The bubble number decrease rate increased on the basis of APG-0814. Within 30 min, the D_{ad} of foam increases from 63.44 μm to 226.28 μm with an increase of 3.57 times.

According to equation (3), a scatter diagram of the D_{ad}^3 and t was drawn and linearly fitted with Ostwald ripening rate as the slope. The gas molecular diffusion coefficient ratio D_{diff} ratio was calculated using the method of Zhu et al. (2019a) based on Ostwald ripening rate of foam formed by APG with different alkyl chain length. D_{diff} ratio can be used to measure the strength of gas molecules in the foam liquid film, and the calculation results are shown in Table 3. When the alkyl chain length increases within a certain range, the D_{diff} ratio gradually decreases. Under the same thermal motion kinetic energy of gas molecules (that is, the same temperature), the mass transfer ability of gas molecules between the lamella gradually weakens and significantly delays the foam decay. When the alkyl chain length increases further (10.9 → 12), the D_{diff} ratio and the foam decay rate increase slightly. The above variation trend further indicates that in the gas transfer from small to large bubbles, the permeability of gas molecules to the lamella of several foaming agent solutions is different. This phenomenon has important relationship with the adsorption amount and the foaming agent molecules arrangements on the lamella. When the foaming agent molecules are sparsely adsorbed on the gas–liquid interface, the gas molecules can easily diffuse into the large bubbles through the lamella. When the foaming agent molecules form a dense adsorption on the gas–liquid interface, the ability of the gas molecules to penetrate the lamella is weakened, and the film can stably lock the gas molecules.

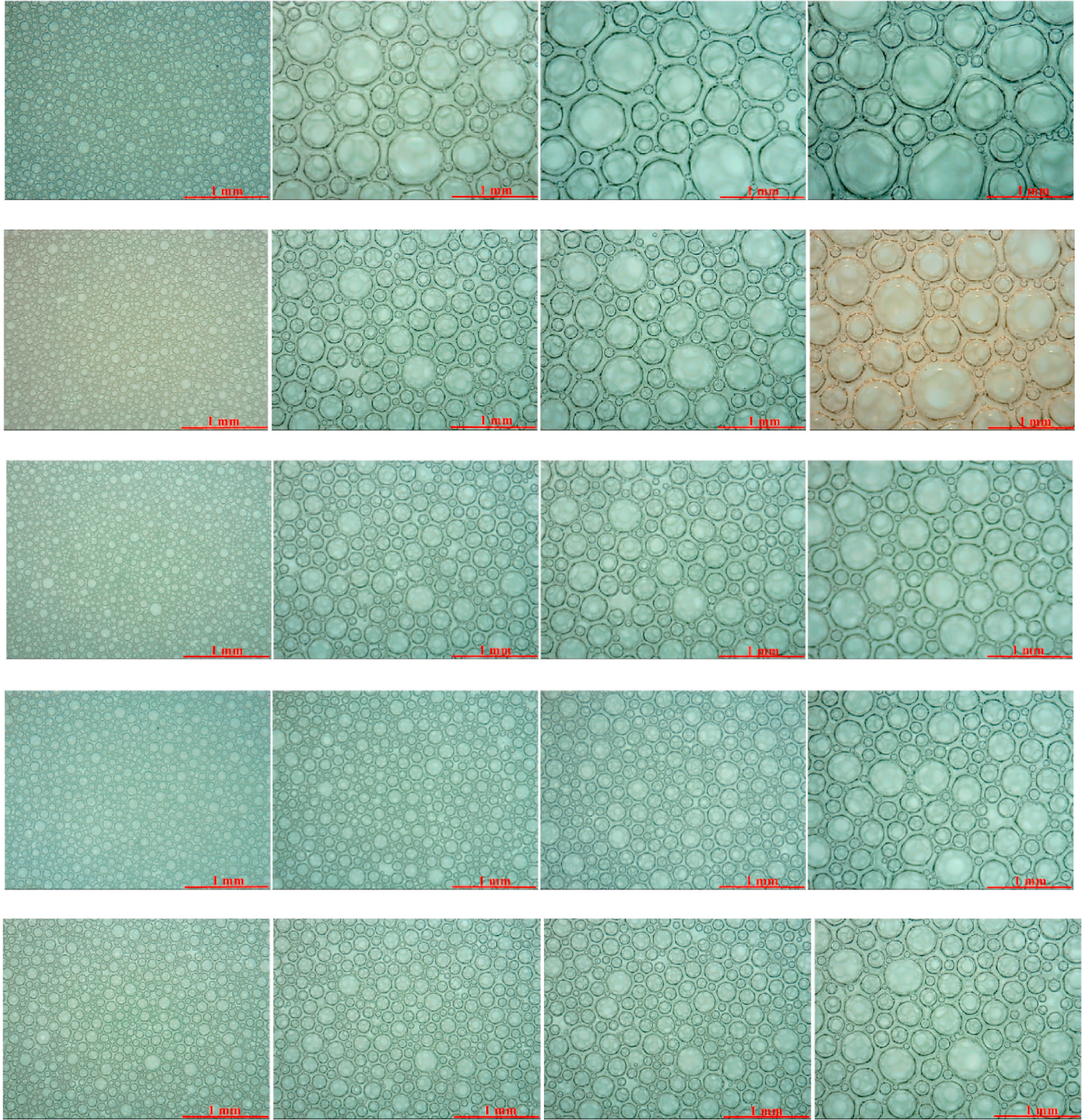


Fig. 5. Foam formed by APG with different alkyl chain lengths: from top to bottom are APG-08, APG-0810, APG-10, APG-0814 and APG-12, from left to right are the coarsening behavior of bubbles at 0 min, 10 min, 20 min and 30 min ($T = 60^\circ\text{C}$).

According to equation (2), the polydispersity coefficient U_{poly} of APG with different alkyl chain lengths during decay was calculated. U_{poly} can be used to describe the non-uniformity of the bubble diameter distribution. A large U_{poly} , indicates the great non-uniformity of the bubble diameter. Fig. 8 shows the U_{poly} variation of APG with different alkyl chain lengths under observation time. Owing to the Ostwald ripening effect (the system tends to most stable state of thermodynamics), the total gas–liquid interface area of the foam system always tends to the minimum value to reduce the Gibbs surface free energy with time. During decay, the internal pressure of the small bubble is higher than

that of the big bubble (according to the Laplace equation, the pressure inside the bubble is inversely proportional to its curvature radius) because the curvature radius of the former is lower than that of the latter. The gas molecules diffuse from small bubbles to large bubbles, thus enlarging the large bubbles but shrinking the small bubbles until they disappear. A large Ostwald ripening rate indicates disproportionation and a high degree of uneven bubble size. When the alkyl chain length of APG is short, the growth rate of U_{poly} in the initial stage is fast. For APG-08, U_{poly} increases from 0.58 to 0.69 in the first 5 min. By 25 min, its U_{poly} increases to 0.89 and then U_{poly} stabilized. For APG-0814,

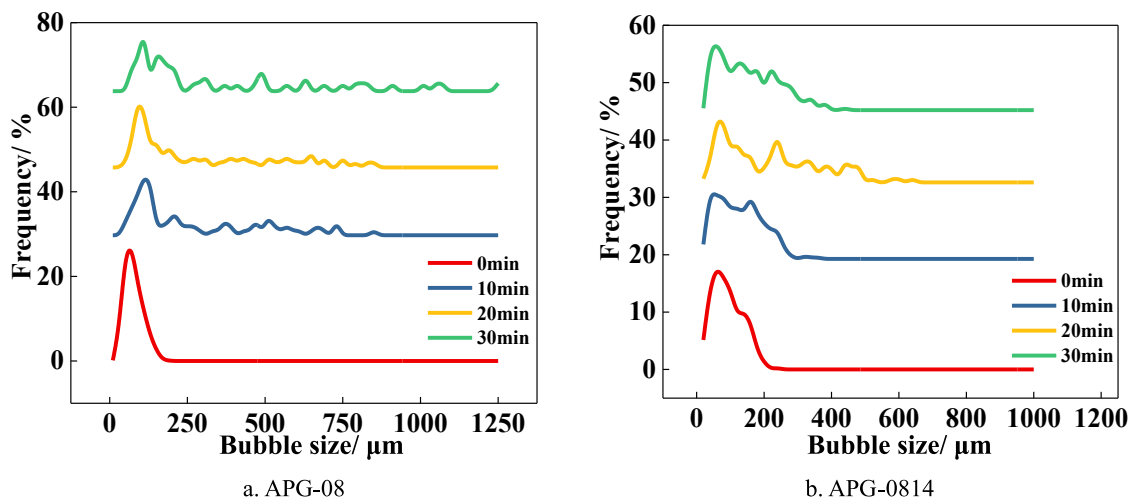


Fig. 6. The variation of bubble diameter distribution during the decay process of foams formed by APG with different alkyl chain lengths, taking APG-08 and APG-0814 as examples ($T = 60^\circ\text{C}$).

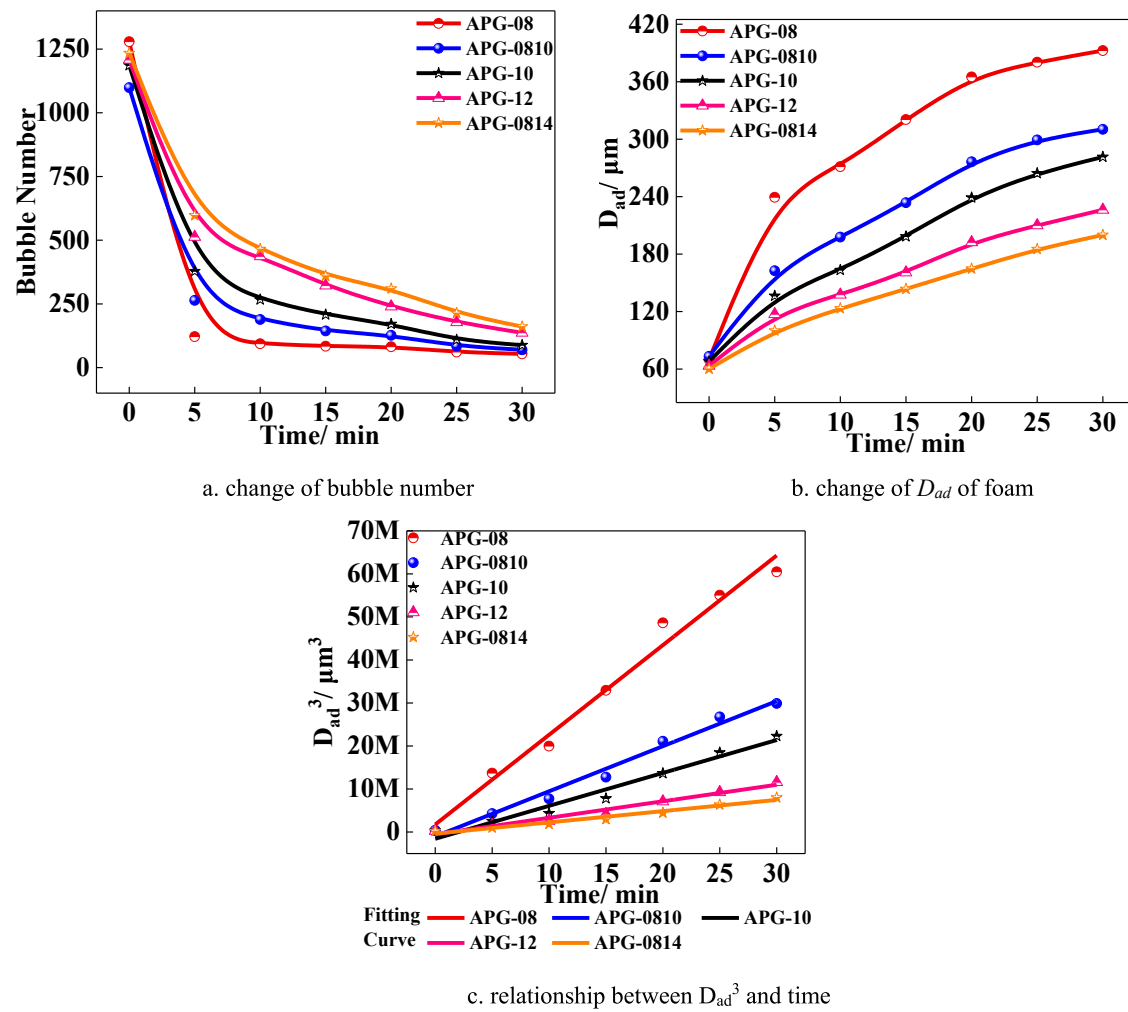


Fig. 7. Changes in the bubble number and D_{ad} of foam formed by APG with different alkyl chain length during the decay process ($T = 60^\circ\text{C}$).

U_{poly} increases from 0.40 to 0.62 and the growth rate is significantly lower than that of APG-08. In terms of U_{poly} changes in the foam system at different times, the irregular degree in the initial time ($t = 0$ min) and in the decay process is consistent with the order of foam drainage rate as follows: APG-08 > APG-0810 > APG-10 > APG-12 > APG-0814. This rule

will be explained by studying the surface adsorbability of APG solutions with different alkyl chain lengths.

Table 3

Ostwald ripening rate and gas molecular diffusion coefficient of foam formed by APG with different alkyl chain length.

Composition	Ostwald Ripening Rate Ω /($\mu\text{m}^3/\text{min}$)	D_{diff} Ratio
APG-08	2.08×10^6	7.97
APG-0810	1.05×10^6	4.01
APG-10	7.65×10^5	2.92
APG-0814	2.62×10^5	1
APG-12	3.84×10^5	1.47

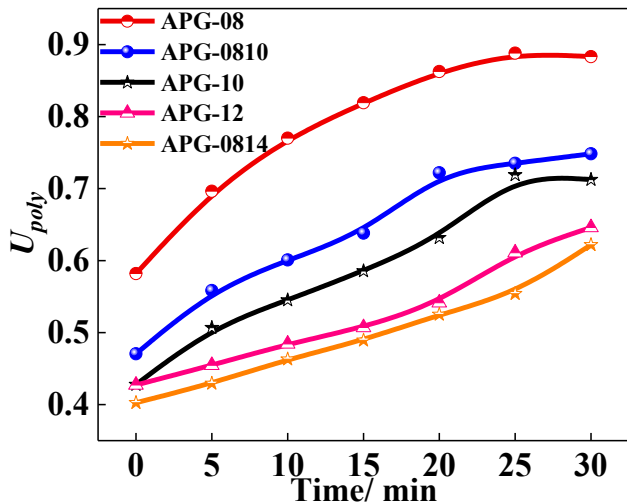


Fig. 8. Variation of polydispersity coefficient of foams formed by APG with different alkyl chain lengths.

3.1.3. Surface adsorption properties of APG with different alkyl chain lengths

APG aqueous solutions with certain concentrations were prepared in distilled water, and the interfacial tension between APG solution and natural gas was measured at 60 °C. The determination results are shown in Fig. 9. With the surfactant concentration increases, the surface tension of each APG first decreases and then gradually stabilizes. Through linear fitting of data points with large decline, a linear equation with high fitting degree is obtained, and the position of the inflection point is the critical micelle concentration (*cmc*). The results showed that within a

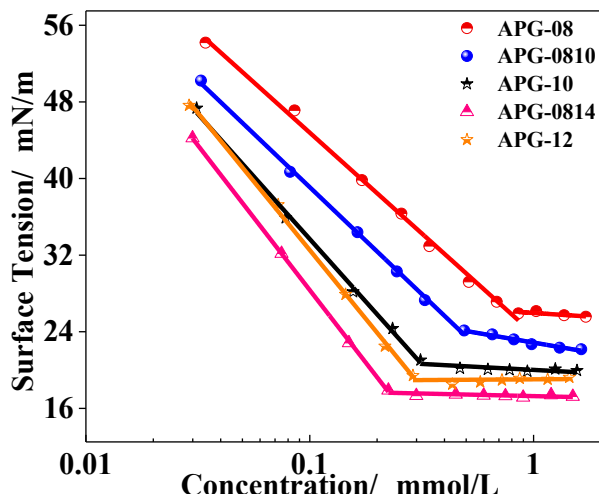


Fig. 9. Relationship between concentration and interfacial tension curves of APG with different alkyl chain lengths (gas phase is natural gas, T = 60 °C).

certain range of alkyl chain length (APG-08→APG-0814), when the chain length of APG increases the surface tension–concentration curve gradually shifts to the lower left, the *cmc* of surfactant and the corresponding surface tension tend to decrease. With further increase in the length (APG-0814→APG-12), the *cmc* and surface tension of the surfactant increase. This finding indicates that the increase of alkyl chain length in a certain range is conducive to the adsorption behavior of APG molecules at the gas–aqueous solution interface, whereas the continuous increase in alkyl chain length weakens the adsorption behavior of surfactants on the gas–liquid interface. This change trend is consistent with the research results for foam drainage and coarsening in sections 3.1.1 and 3.1.2. The slope of the fitted curve can be obtained ($\frac{d\sigma}{d \ln c}$) by linearly fitting the decreasing interval of the surface tension–concentration curve (Fig. 9). The A occupied by surfactant molecules in the adsorption layer was calculated according to the Gibbs equation (equation (5)) (Eastoe and Dalton, 2000), and the fitting results are shown in Table 4.

$$A = \frac{1}{T N_A} = \frac{-nRT}{N_A} \left(\frac{d\sigma}{d \ln c} \right)^{-1} \quad (11)$$

In equation (11), R is the ideal gas constant (8.314 J/mol·K), T is the Kelvin temperature (K), N_A is the Avogadro constant (6.02×10^{23}), and c is the molar concentration of surfactant (mmol/L). When the surfactant is for non-ionic type, the value of n is 1 (Zana, 2002).

The surface pressure (π) of APG series surfactants can be calculated by using equation (12) to further understand the adsorption capability of surfactants at the gas–liquid interface.

$$\pi = \sigma_0 - \sigma_m \quad (12)$$

The minimum adsorption surface area and surface pressure of APG molecules with different alkyl chain lengths can be calculated using equations (11) and (12), and the results are shown in Fig. 10. When the alkyl chain grows within a numerical range, the π increases linearly, but the A decrease linearly. This phenomenon occurs because the increase in methylene in the alkyl chain enhances the hydrophobicity of the surfactant and consequently enhancing the driving force for the formation of the surface adsorption layer (Verga et al., 2012). The adsorption tendency of APG molecules from the bulk phase to the gas–liquid interface increases with the growth of the alkyl chain length to escape the polar environment in the water phase. APG molecules containing a large amount of methylene groups on the alkyl chain are easily adsorbed at the gas–liquid interface, thus forming a relatively saturated adsorption layer. In addition, the surface area occupied by each APG molecule tends to decrease due to the increase in surface adsorption potential. Within a certain range, when the APG alkyl chain is long, the adsorption capability is strong, and the A is low. These conditions are conducive to the formation of tight surfactant molecular layer. However, with the continuous growth of APG alkyl chains, the occupied area of APG molecules on the gas–liquid interface increases and the number of APG molecules on the gas–liquid interface is reduced. The adsorption of APG molecules on the gas–liquid interface becomes sparse again, resulting in a decrease in APG-12 ability to reduce the gas–liquid interface tension.

According to Gibbs function, the external energy of natural gas foam system decreases first and then increases. First, the increase in APG alkyl chain within a certain range enhances the stability of natural gas foam prepared by APG from the surface energy. Second, the differential

Table 4

Fitting results of the relation curve of concentration and surface tension (T = 60 °C).

Composition	Fitting Equations	Correlation Coefficient R^2
APG-08	$\sigma = -21.0254 \ln c + 23.7649$	0.9967
APG-0810	$\sigma = -22.3128 \ln c + 16.7835$	0.9989
APG-10	$\sigma = -26.1189 \ln c + 7.5659$	0.9978
APG-0814	$\sigma = -30.2470 \ln c - 1.8947$	0.9998
APG-12	$\sigma = -28.6653 \ln c + 3.8624$	0.9986

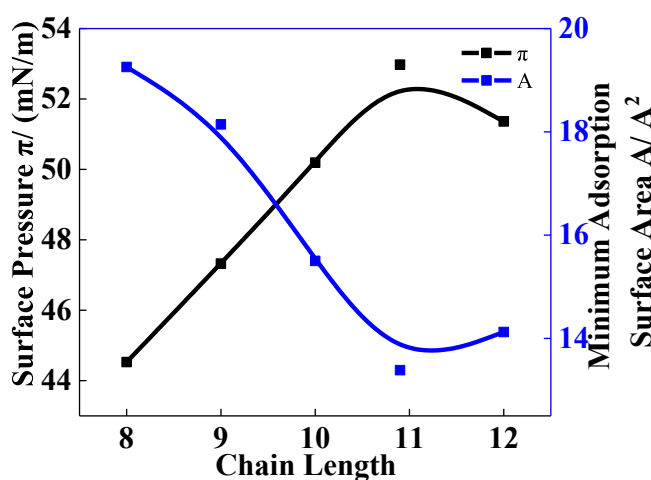


Fig. 10. π and A of APG with different alkyl chains lengths ($T = 60^\circ\text{C}$).

pressure between bubbles is proportional to the surface tension, and the low surface tension can reduce the driving force of bubble coarsening and delay defoaming to some extent. Third, the adsorption capacity and concentration of foaming agent molecules on the gas–liquid interface also determine the permeability of gas molecules to the liquid film.

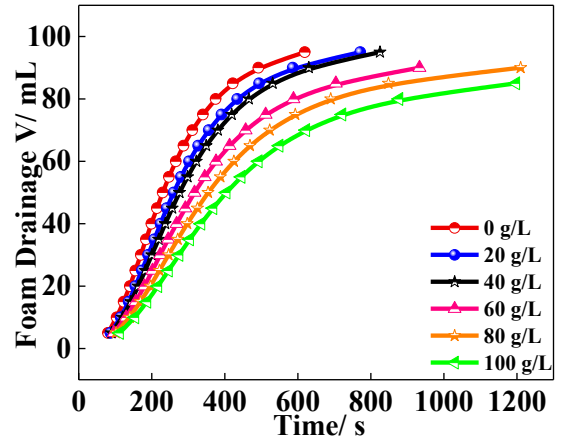
When the adsorption density of APG molecules with different carbon chain lengths at the gas–liquid interface is high, the internal gas molecules are difficult to transfer to other bubbles. This finding also corresponds to the coarsening behavior of the APG foam. These three reasons leads to the differences in the decay of foam prepared by APG with different alkyl chain lengths.

3.2. Effect of metal ion valence on APG foam decay process

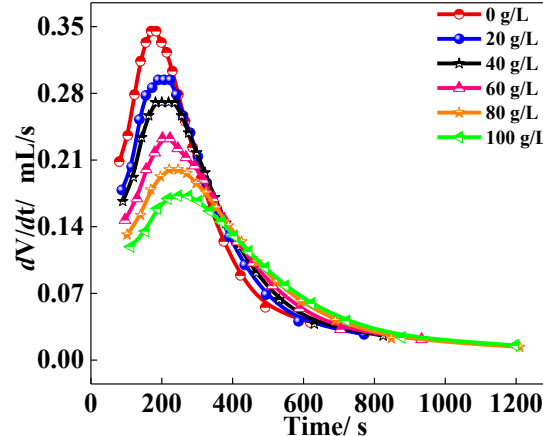
Metal ions have a significant impact on the surfactants performance, in the formation water and produced water of most oilfields, the most common cations contains Na^+ , Ca^{2+} and Mg^{2+} , this study takes Na^+ and Ca^{2+} as examples to study the effect of metal ions valence and its concentration on the APG foam performance. Given that the drainage volume–time curves at different temperatures were basically similar, the formula in 3.1.1 (equations (4), (7) and (10)) was still used to analyze the influence of metal ions in different valences during foam drainage (changes in drainage activation energy and rate). The drainage volume–time curves of NaCl and CaCl_2 at different temperatures (see Figs S4 and S5) and the values of the model parameters V_{max} , K and n obtained by fitting the drainage volume–time curves with Hill function (equation (4)) are provided in Supplementary Materials (see Tabs S1 and S2).

3.2.1. Effect of metal ion valence on APG foam drainage kinetics

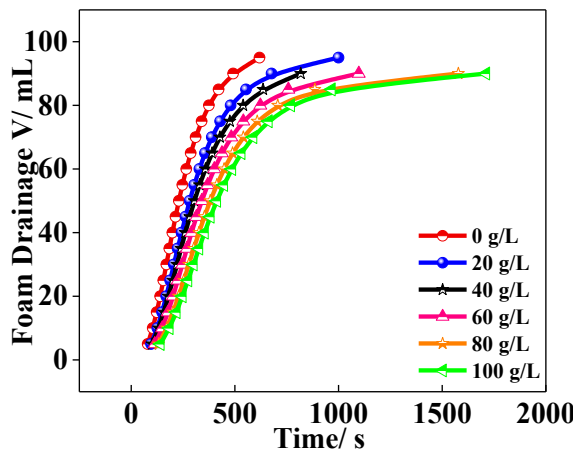
Since the influence of NaCl and CaCl_2 on the foam drainage process is



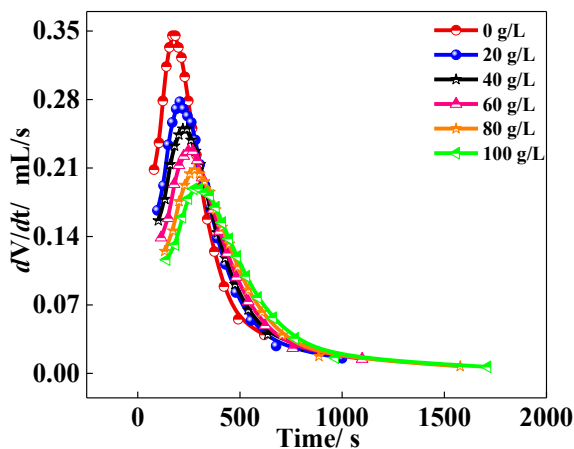
a. NaCl (drainage volume-time curves)



b. NaCl (drainage rate-time curves)



c. CaCl_2 (drainage volume-time curves)



d. CaCl_2 (drainage rate-time curves)

Fig. 11. Effect of metal ions valence on the drainage process of natural gas foam ($T = 60^\circ\text{C}$).

basically the same at different temperatures, this section only takes the ambient temperature of 60 °C as an example to elaborate the influence of metal ions on the natural gas foam system. The corresponding drainage volume-time curve and drainage rate-time are shown in Fig. 11. The stability of foam system prepared by different valences is enhanced with the increase in salinity. This phenomenon becomes highly evident when the valence state of metal ions is high. According to the conclusions obtained in 3.1.1, the main phase that determines the drainage rate of foam system is the control phase, that is, when the foam systems starts to drain until the maximum value. In the foam prepared with the same inorganic salt, the maximum value of the drainage rate of the foam system gradually decreases and the time requires for reaching the maximum value expanded. The maximum value of foam system was calculated under different conditions and its occurrence time (Fig. 12). With the increase in metal ion valence, the occurrence time of maximum value of drainage rate also increases, but the maximum value of drainage rate has dropped. When the salinity is higher than 60 g/L, the maximum value of drainage rate changes in an opposite trend: that is, a large metal ion valence leads to a large the maximum value of the drainage rate. Under 80 g/L salinity, the maximum values of the drainage rate of the foam prepared by NaCl and CaCl₂ are 0.2 and 0.2083 mL/s occurring at 246 and 278 s, respectively. Compared with the slight increase in the maximum drainage rate, the time of the maximum has significantly gone backward. Therefore, this phenomenon does not fundamentally change the influence of metal ion valence on the stability of foam system.

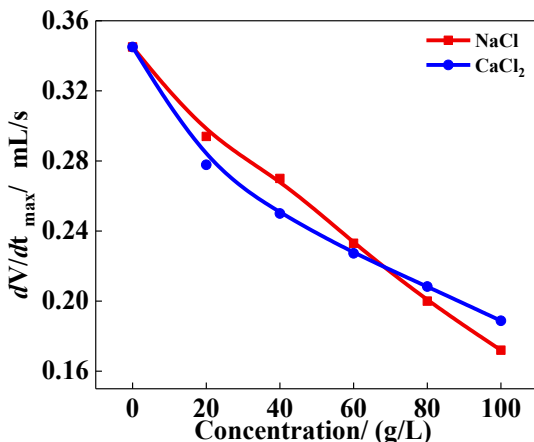
The parameters obtained from equation (4) can be substituted into equation (8) to calculate the drainage rate constants of metal ions in different valences at various temperatures. The curve of relationship between $\ln k_d$ and T^{-1} based on obtained data is shown in Fig. 13-a and b, and the variation trend of E_a with the increase of salinity is shown in Fig. 13-c. The relationship between $\ln k_d$ and T^{-1} revealed that as the increase in salinity and ionic valence, the k_d decreases continuously. A high valence indicates great sensitivity of the drainage rate to the temperature change. Under the same salinity, the E_a of the foam drainage is high when the ionic valence is high. Therefore, the foam system prepared by high-valence metal ions must overcome a large energy barrier during drainage. This phenomenon can be explained by studying the adsorption properties of APG molecules in aqueous solutions of metal ions with different valences (see section 3.2.3).

3.2.2. Effects of metal ions on the coarsening behavior of APG foam

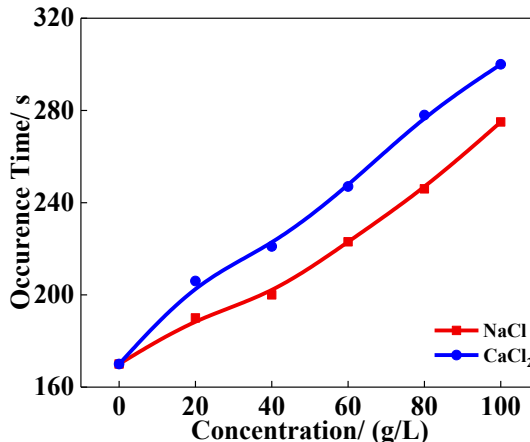
The images of the coarsening of APG foam prepared from different valence metal ions are shown in the Supplementary Materials (see Figs S6 and S7). Changes in the bubble number, diameter distribution, and

average bubble diameter of APG foam under different valence ions were analyzed by Nanomeasure software. The variation of foam diameter distribution at different concentrations (20 and 100 g/L) of metal ions in different valence are shown in Fig. 14. The PSD of foam in the initial state ($t = 0$ min) is relatively concentrated. The initial diameter range of bubbles is 20–160 μm, and the PSD curve is unimodal. With the coarsening of the foam system, the foam size has gradually differentiated, and the distribution frequency of bubbles with small sizes is significantly decreased. When the gas molecules diffuse to large bubbles, the bubbles size increases, and the curve exhibits a certain frequency distribution in the range of large particle size and gradually becomes multi-peak. For the metal ions in different valences, the degree of dispersion of foam diameter distribution can be alleviated to some extent by increasing the prepared water. With NaCl as an example, when the salinity is 100 g/L, the frequency distribution of the bubble size is only within the range of <400 μm and becomes 0 ($t = 30$ min) within the range the range of >400 μm. Compared with the salinity of 20 g/L, under the same observation time, a certain distribution of foam size occurs at 400–760 μm (the distribution frequency sums up to 27.03%). The coarsening rate of foam decreased with the increase in salinity. When the valence of metal ions increases, the diffusion ability of gas molecules in the foam film decreases, and the behavior of foam coarsening can be effectively delayed. At 30 min, the distribution frequency of APG foam prepared by NaCl is only 30.80% in the range of 0–100 μm, and 53.74% in the range of 0–200 μm. Most of the gas molecules have been transferred from small to large bubbles, thus compressing the distribution frequency of small bubbles. For the foam prepared by CaCl₂, the distribution frequency is 34.95% in the range of 0–100 μm and 57.80% in the range of 0–200 μm. When the metal ion valence increases, the behavior of mass transfer of gas molecules to large bubbles can be alleviated to some extent. The distribution frequency of small bubbles increases with the metal ion valence and effectively reduces the distribution frequency of large bubbles. High-valence metal ions enhance the dense distribution of APG molecules at the gas–liquid interface and hinder the mass transfer of gas molecules between bubbles.

The changes in the bubble numbers and the D_{ad} of bubbles prepared by different brine (different inorganic salt and salinity) were also analyzed during decay. The statistical results are shown in Fig. 15. Fig. 15-a and c show that the bubble number significantly declines in the initial stage (0–5 min). In 5–10 min, the decline rate of the bubble number is significantly smaller compared with that in the initial stage but still maintains a fast rate. After 10 min, the decline rate of bubble number is further reduced until it stabilizes. For the APG foams prepared by the brine with different valence metal ions, with the increase in salinity, the decline rate of bubble number in each stage is alleviated to



a. occurrence time of maximum drainage rate



b. maximum drainage rate

Fig. 12. Maximum drainage rate and its occurrence time of foam prepared by different metal ions valence ($T = 60$ °C).

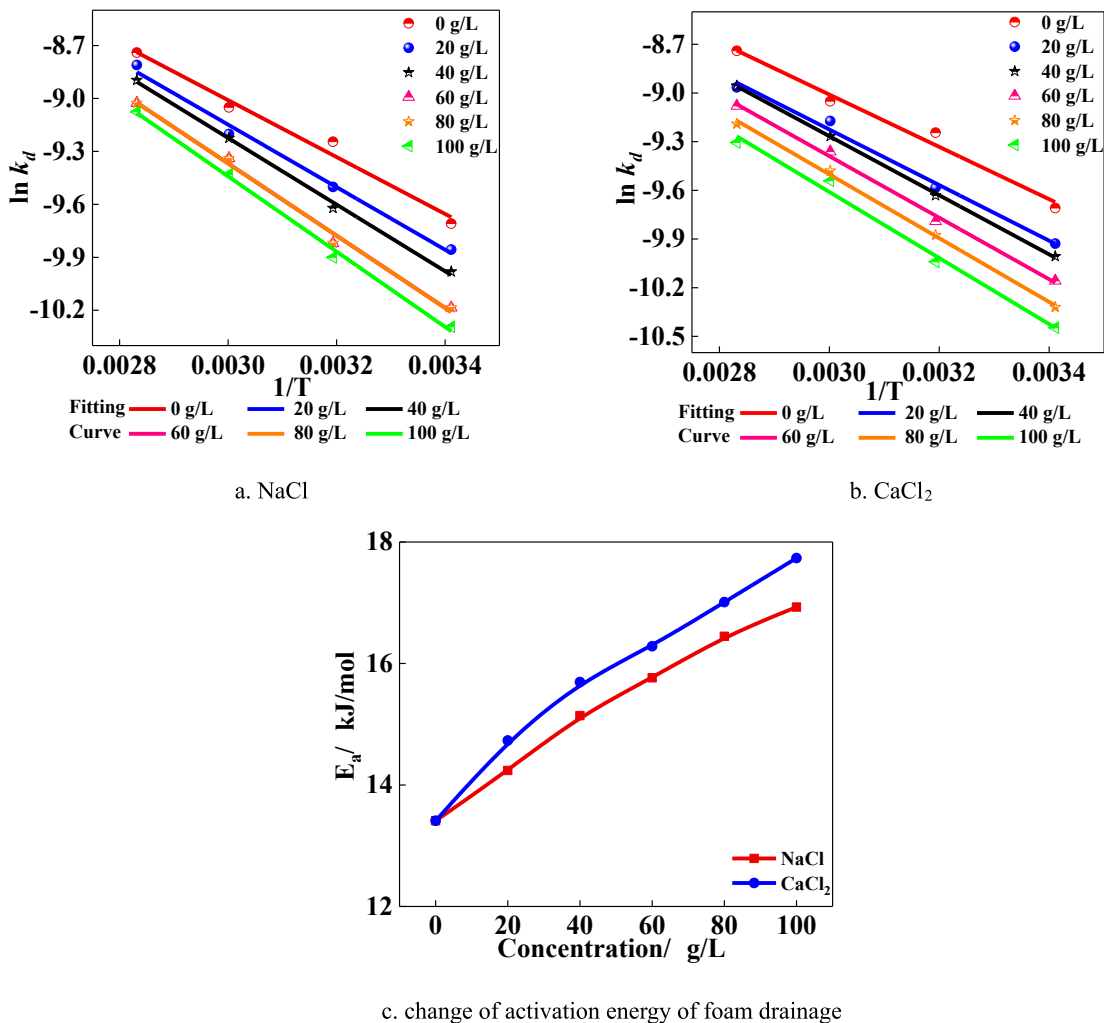


Fig. 13. Changes of Arrhenius fitting curves and activation energy of foam drainage ($T = 60^\circ\text{C}$).

varying degrees. For the APG foam prepared by NaCl, when the salinity is 20 g/L, the bubble number decreases from 1164 to 380 at 67.35% in the first 5 min and to 111 at 90.46% in 30 min. When the salinity increases to 100 g/L, the bubble number drops from 1354 to 462 in the same time ($t = 5 \text{ min}$), and the decrease rate is reduced to 65.88%. At 30 min, the bubble number decreases to 189 with a decrease of 86.04%. The bubble coarsening is weakened to some extent, and this mitigated phenomenon becomes apparent with the increase in metal ion salinity. For the APG foam prepared by CaCl₂, when its salinity is 100 g/L, the bubble number decreases from 1224 to 503 with a decrease of only 58.91% in the first 5 min and to 178 with a decrease of only 82.27% in 30 min. With the increase in metal ion valence, the decay behavior of foam system can be further delayed.

For the same type of inorganic salt, with the increase in salinity, the increase of D_{ad} of the foam system decreases. For NaCl, when the salinity is 20 g/L, the D_{ad} of foam increases from 80.45 μm to 145.43 μm , with an increase of 1.81 times in first 5 min and then to 258.83 μm with an increase of 3.22 times in 30 min. When the salinity increases to 100 g/L, the D_{ad} only increases from 72.30 μm to 114 μm with an increase of 1.58 times in the first 5 min and then to 205.79 μm , with an increase of 2.85 times in 30 min. With the increase in metal ions valence, the increase in bubble size can be further slowed down. For the APG foam prepared by CaCl₂ in same salinity (100 g/L), the D_{ad} increases from 69.20 μm to 110.04 μm in the first 5 min, but the increase rate has decreased to 1.59 times. The D_{ad} only increases to 197.05 μm in the 30 min, the rate is reduced to 1.79 times. Compared with that of the APG foam prepared by

NaCl of the same salinity, the foam coarsening rate is significantly decreased, and the stability is improved.

The fitting curves of D_{ad}^3 -time of APG foam prepared by different valence metal ions under different salinities are shown in Fig. 16-a and b. Fig. 16-c shows the Ostwald ripening rate of different metal ions (slope of the fitting curve). With the increase in salinity in the APG solution, the coarsening rate of foam system decreases to different degrees. When the salinity increases from 0 g/L to 100 g/L, the ripening rates of APG foam prepared by three inorganic salts all experience two stages of rapid decline (0–20 g/L) and linear decline (20–100 g/L). However, the decline degree of the ripening rate increases significantly with the ion valence. When the salinity of the APG solution is 0 (blank group), the ripening rate of foam system is $7.41 \times 10^5 \mu\text{m}^3/\text{min}$. When the salinity increases to 100 g/L, the ripening rates of NaCl and CaCl₂ decreased to 2.87×10^5 and $2.28 \times 10^5 \mu\text{m}^3/\text{min}$, respectively, with decreases of 61.27% and 69.23%, respectively. The reduction of the ripening rate reflects the decrease in the diffusion rate of the gas molecules. When the metal ion valence and salinity of the foam film increase, the kinetics of bubble coarsening can be weakened, thus hindering the diffusion of gas molecules. Fig. 16-d shows that the D_{diff} ratio decreases significantly with the increase in metal ion valence and salinity. Owing to the attraction of metal ions, the free energy of water molecules in the brine decreases, thus reducing the rate of the water molecules escaping from the gas-liquid surface. In a macroscopically perspective, the saturated vapor pressure on the surface of liquid film decreases. This phenomenon becomes evident when the metal ions increases and eventually leads to a

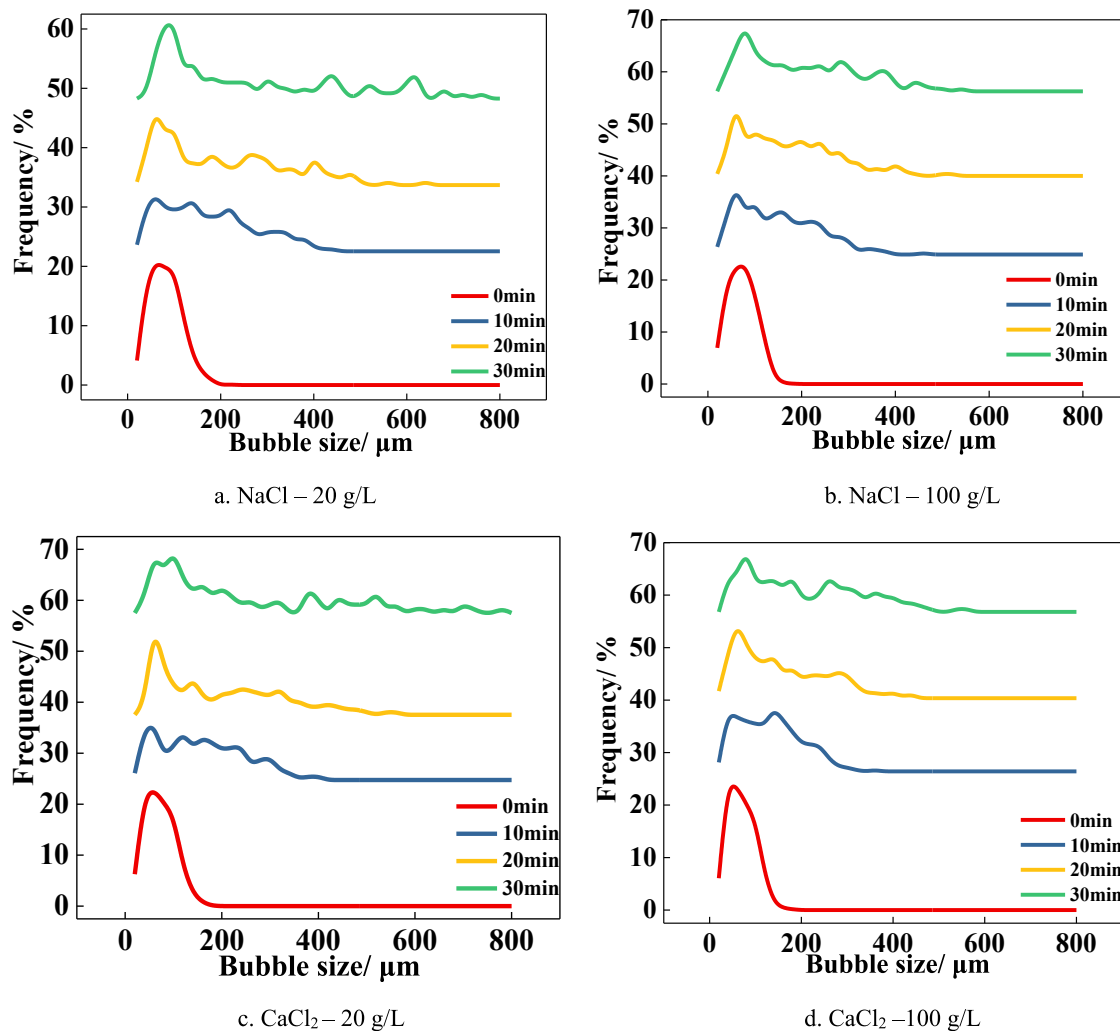


Fig. 14. The change of bubble size distribution during the decay of APG foam with different valence metal ions ($T = 60^\circ\text{C}$).

decrease in the mass transfer rate of the liquid film with the increase in salinity and metal ion valence (Calder and Neal, 1983), and the rate of bubble coarsening decreases.

The variation of U_{poly} of APG foam system with different valence metal ions is shown in Fig. 17. With the increase in salinity, the U_{poly} of foam decreases at the initial stage (0 min). With time, the gas molecule diffusion in the foam film has enhanced the unevenness of the bubble size distribution to varying degrees. When the salinity of the APG solution is 100 g/L, the U_{poly} of the foam systems prepared by NaCl and CaCl₂ increases to 0.62 and 0.58, respectively, during the observation time ($t = 30$ min). This finding indicates that APG can form bubbles with uniform and fine scales under high-salinity and high-valence metal ions. According to the Laplace equation, bubbles with close curvature (with relatively low U_{poly}) can reduce the mass transfer of gas molecules between bubbles, thereby further explaining the low coarsening rate and good stability of APG foam with high-salinity and high-valence metal ions.

3.2.3. Surface adsorption properties of APG with different valence metal ions

The effects of different valence metal ions on the surface tension between APG-10 solution and natural gas are shown in Fig. 18-a and b. The cmc of APG-10 in different inorganic salt solutions can be obtained by fitting the scatter points before and after the surface tension inflection point. Within the range of salinity in this paper, and in the same type of brine, the cmc of APG-10 and the surface tension at equilibrium decrease

to different degrees with the increase in inorganic salt concentration, and the effect is amplified by the increase in metal ion valence. The π and A of APG-10 under different conditions can be calculated according to equations (11) and (12), and the results are shown in Fig. 19-a and b. When the solution salinity increases, the π also increases continuously. On the one hand, the strong hydrophilic glycoside groups increases the hydrophilicity of the surfactant to maintain good water solubility in high-salinity conditions. On the other hand, as inorganic electrolytes, NaCl and CaCl₂ form competitive hydration (salting out effect) with APG in aqueous solution, shield the interaction between surfactants and water molecules, reduce the repulsion between APG molecules, and thus improve the adsorption capability of APG molecules at the surface (Stubenrauch et al., 2017). Fig. 19-b shows that with the increase in salinity, the A of APG molecules at the gas–liquid interface decreases monotonically, indicating the increase in adsorption sites of surfactant molecules at the gas–liquid interface increase (that is, the adsorption density rises) and the formation of dense surfactant molecules that are beneficial to improve the stability of the foam (Wang et al., 2016). Jhan et al. (2014) reported that water molecules are often surrounded by the metal ions in brine, thus foaming the aggregations of water and salt. This phenomenon results in a large concentration of water molecules in the foam liquid film. Owing to the adsorption and aggregation of inorganic salts on the liquid film, the structure of the foam film becomes thick, and the structural strength of the liquid film is enhanced, thus improving the stability of the foam. Similar conclusion was reported by Sun et al. (2016), with the increase in brine salinity, the thickness of liquid film

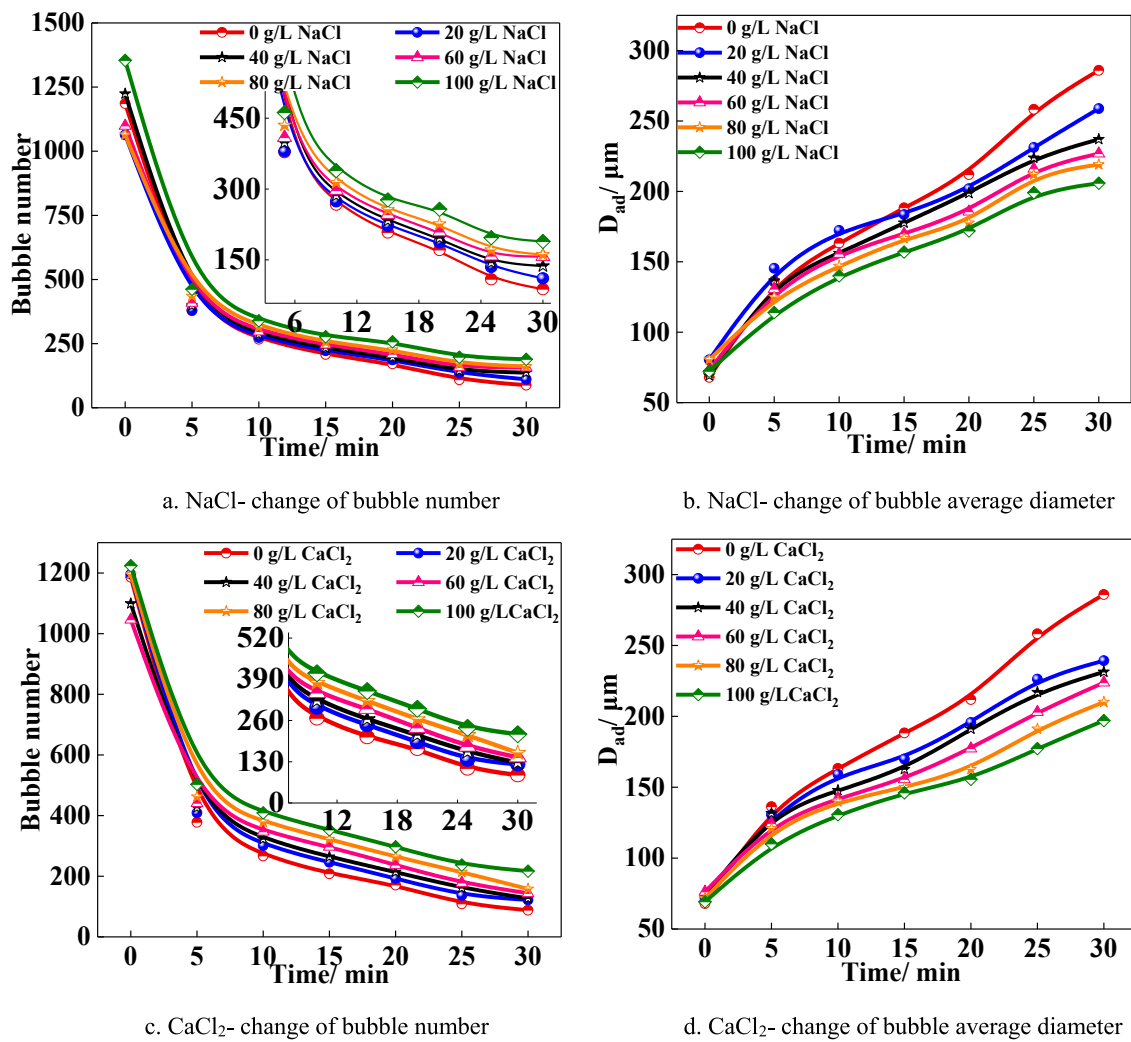


Fig. 15. Changes in bubble number and D_{ad} of bubbles during the decay of APG foam with different valence metal ions ($T = 60$ °C).

increases as shown in the scanning electron microscope photographs. When the solution salinity increases from 100 to 200 g/L, the foam film thickness increases from 27.14 to 39.37 μm. With the increase in metal ions valence, the radius of metal ions also increases. At the same salinity, the ability of high-valence metal ions to shield the interaction between surfactants and water molecules is evident, and their ability to reduce the repulsion between APG molecules is large. These characteristics improve the adsorption capability of APG molecules on the gas-liquid interface and the stability of the foam system. Therefore, in high-salinity conditions, the stability mechanism of APG foam corresponds to the increase in salinity and metal ion valence, APG molecules can be formed on the gas-liquid interface of dense and orderly the molecular layer. The increase in brine salinity is beneficial to the increase in liquid film thickness. As a result, a strong surface adsorption layer is formed, and the resulting foam film has high strength, thereby delaying the drainage of natural gas foam and enhancing the stability of the foam system.

3.3. Effect of polymer on APG foam decay process

The effects of DG, XG, and KYPAM-6s on the natural gas foam decay were studied. As the drainage volume-time curve of the foam is basically similar at different temperatures, the equation in section 3.1.1 (equations (4), (7) and (10)) was still used to analyze the influence of polymer on the foam drainage (change of drainage activation energy and drainage rate). The curves of drainage volume-time at different

temperatures (see Figs S8, S9 and S10) and the values of the parameters V_{max} , K and n obtained by fitting the drainage volume-time curves with equation (4) are shown in the Supplementary Materials (see Tabs S4, S5 and S6).

3.3.1. Effect of polymer on APG foam drainage kinetics

According to the drainage liquid-time curve of the foam system (Fig. 20-a, c and e), the stability of the foam system is enhanced to varying degrees with the increase in polymer concentration. With the increase of polymer concentration, the maximum drainage rate of the foam system decreases significantly, and the time of maximum drainage rate occurrence is also significantly increased. When DG is only 0.10 g/L, the maximum drainage rate decreases from 0.3452 mL/s to 0.1819 mL/s, and the time of maximum drainage rate occurrence increases from 170 s to 305 s. When the DG concentration increases to 0.75 g/L, the drainage rate curve is extended from a sharp peak curve to a broad peak curve. The maximum value of drainage rate is reduced to 0.0746 mL/s, and the occurrence time of this value is delayed to 605 s, which effectively reduces the drainage rate of the control stage in the foam drainage. The performance of XG stabilized foam is between that of DG and KYPAM-6s, but the foam stabilization effect is still evident. When the concentration of XG is 0.1 g/L, the maximum drainage rate drops to 0.2327 mL/s, and the time of this value occurrence is delayed to 235 s. Moreover, when the concentration of XG continues to increase, the foam stabilization effect of XG is close to that of DG. KYPAM-6s has the worst foam stabilization effect. When the KYPAM-6s concentration increases,

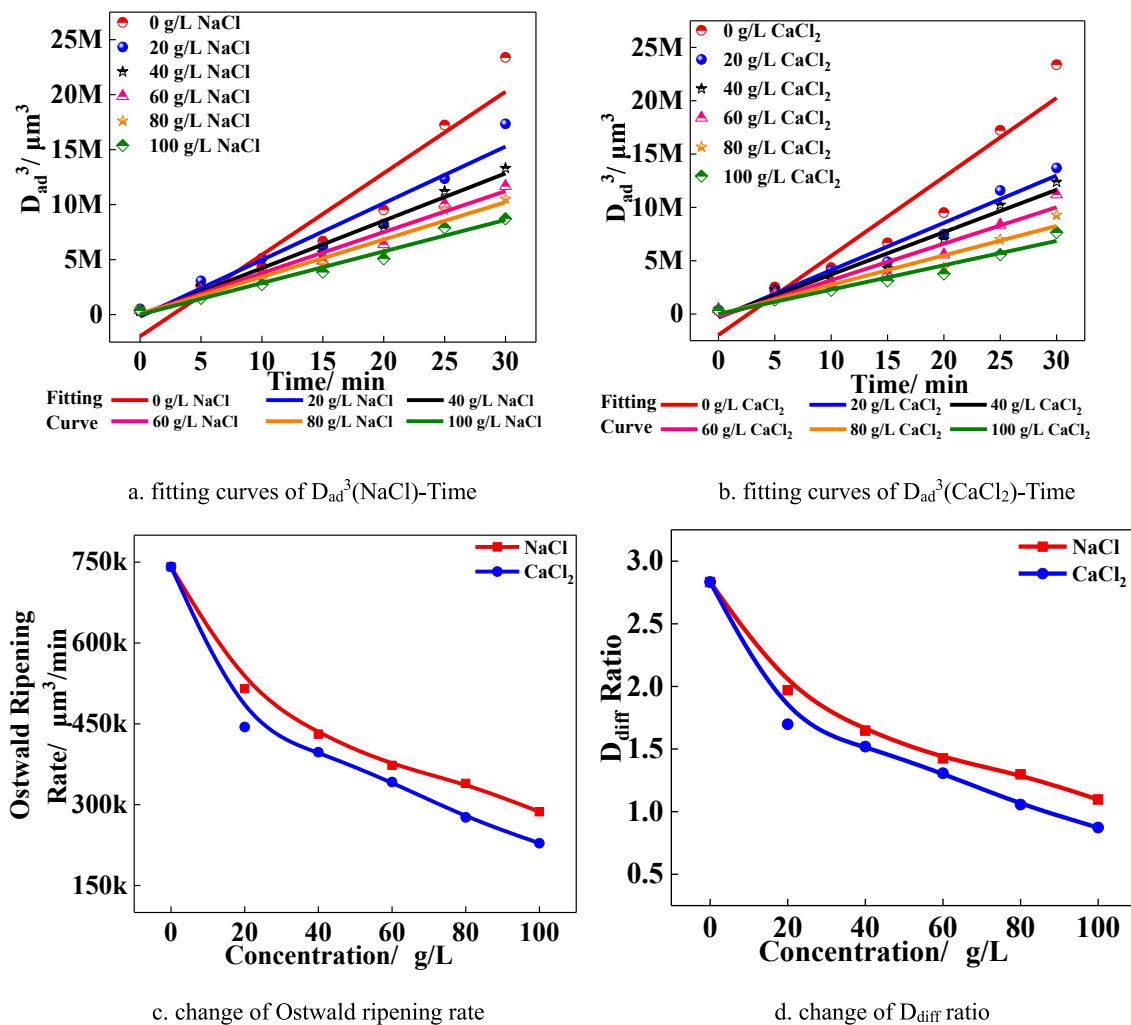


Fig. 16. Changes of Ostwald ripening rate and D_{diff} ratio during APG foam decay with different valence metal ions.

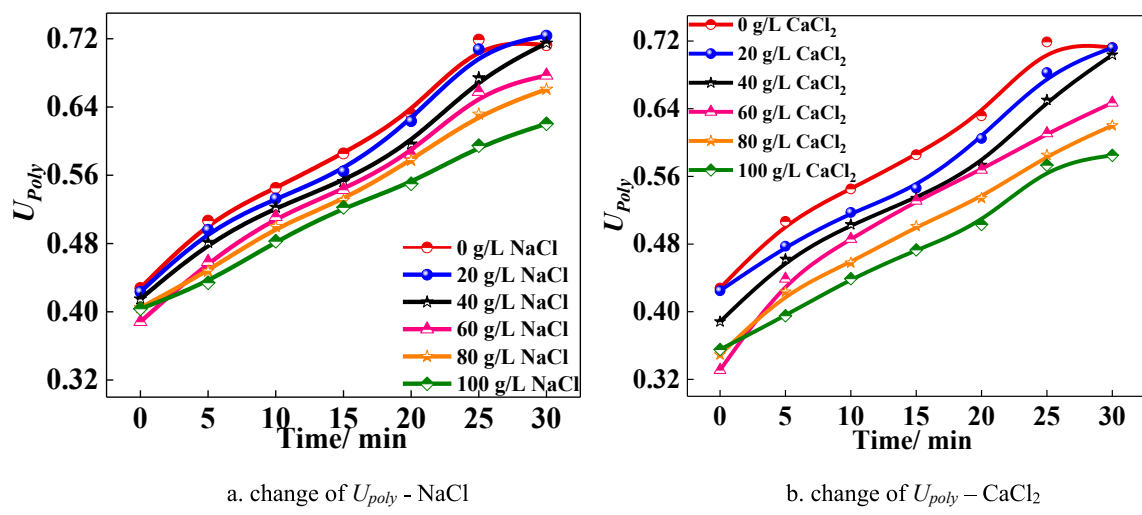


Fig. 17. Changes of U_{poly} during APG foam decay with different valence metal ions.

it cannot effectively delay the time when the maximum drainage rate appears (Fig. 21-a). When the KYPAM-6s concentration increases from 0.10 g/L to 0.75 g/L, the occurrence time of the maximum drainage rate is delayed from 198 s to 231 s with no significantly increase. Although

the maximum drainage rate is reduced from 0.2778 mL/s to 0.2223 mL/s, the decrease is significantly lower than that of XG and DG, and the drainage rate curve was still presents a sharp curve. In general, the foam stabilization effect of KYPAM-6s is the worst. In a certain concentration

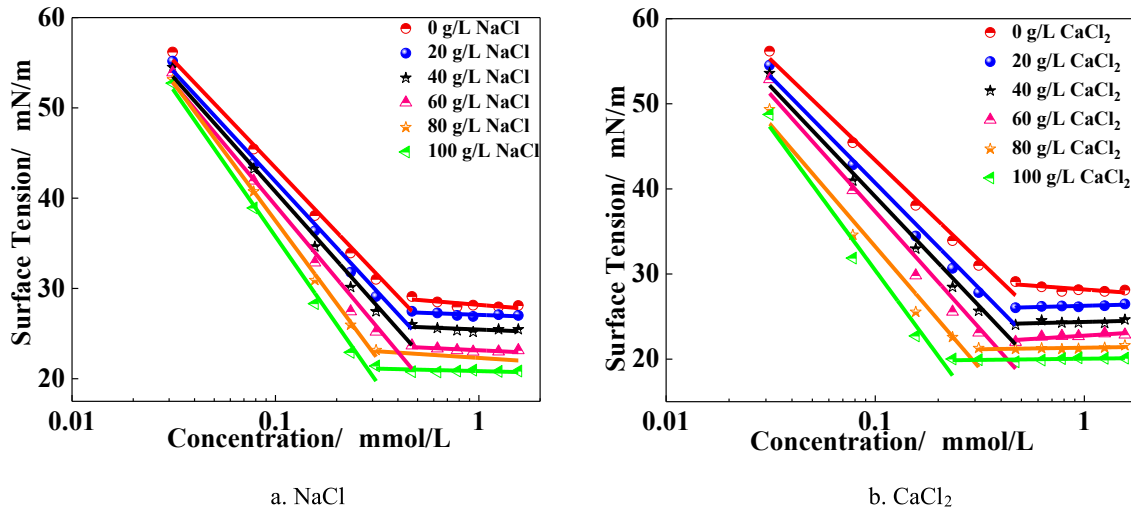


Fig. 18. Change of surface tension of APG-10 solution with different valence metal ions (gas phase is natural gas, $T = 60^\circ\text{C}$).

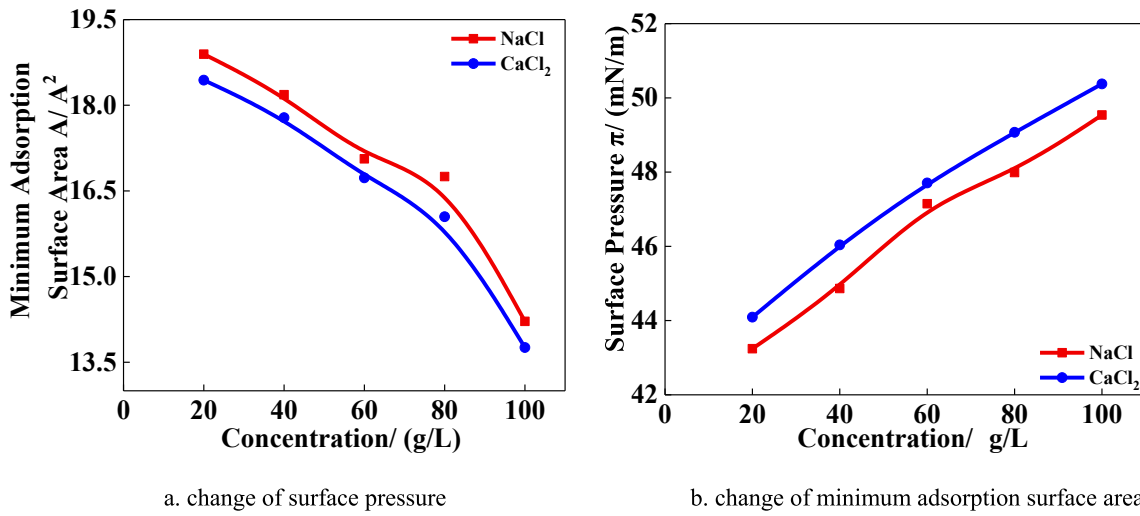


Fig. 19. Change of surface adsorption of APG-10 solution with different valence metal ions.

range (0.10–0.25 g/L), the foam stabilization effect of DG is higher than that of XG. Beyond this concentration range, the foam stabilization effects of DG is close to that of XG.

The parameters obtained after fitting with equation (4) can be substituted into equation (8) to calculate the k_d of different polymers at different temperatures. The curve of relationship between $\ln k_d$ and T^{-1} is shown in Fig. 22-a, b and c, and the variation trend of E_a with the increase in concentration is shown in Fig. 22-d. At the same concentration, with the increase in ambient temperature, the sensitivity of the k_d of the three polymers to temperature is in the order of DG > XG > KYPAM-6s. With the temperature decrease, the k_d of DG decreases faster (the drainage rate becomes smaller). By contrast, the decrease in the k_d of KYPAM-6s is lower than that of DG. According to the Arrhenius equation, the E_a of the enhanced foam system formed by three types of polymers can be calculated. Under the same conditions, the E_a of the drainage of DG is the largest, and the foam system formed by DG needs to overcome a larger energy barrier during drainage to enhance the stability of the foam system. The E_a of KYPAM-6s foam is the lowest, and the corresponding foam stabilization effect is also poor.

3.3.2. Effects of polymers on the coarsening behavior of APG foam

The images of APG foam coarsening with different polymers combinations are shown in Supplementary Materials (see Figs S11, S12 and

S13). The changes in bubble number, bubble size distribution, and D_{ad} of the APG foam obtained by Nanomeasure software were analyzed. The diameter distribution during the decay of enhanced foams of different polymers is shown in Fig. 23. The PSD curve of the foam is still changing from the unimodal shape in the initial stage to the multimodal shape in the later period. In general, the stability of APG foam with the added polymer is higher than that of inorganic salts. In the same observation time, the size transition from small to large is restrained as manifested by the PSD curve appearing as a wide peak (platform region) in the range of small size during the later decay process. With the increase in polymer concentration, the PSD curve maintains wide peak at small size for long time. When KYPAM-6s is 0.10 g/L, two platform regions (size range 110–140 μm and 199–260 μm) appear at 10 min with corresponding distribution frequencies of 6.80% and 4.77%, respectively. After 10 min, the platform region in these two particle size ranges disappear, and the platform region expands to large particle size when the gas molecules are diffused into the large bubbles. At 30 min, one platform region is located at 162–394 μm (frequency 2.25%), and the other platform region is located at 540–577 μm (frequency 0.90%). When KYPAM-6s concentration increases to 0.75 g/L, a long platform region (40–130 μm) appears in the small size region at 10 min with a frequency of 11.53%. Although the platform region in this range disappears in the later stage of observation time ($t = 30$ min), the maximum

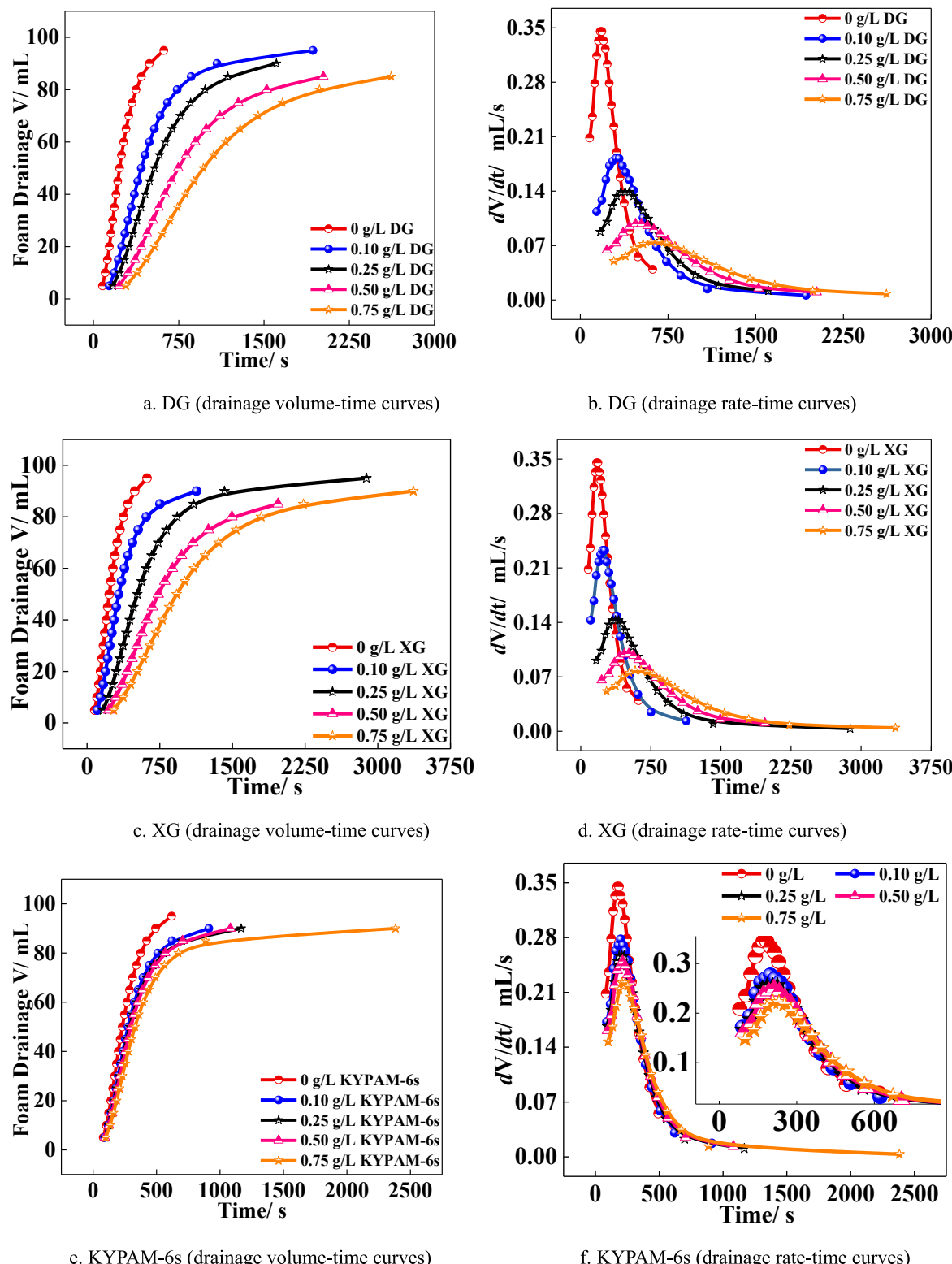


Fig. 20. Effect of polymer on the drainage process of natural gas foam ($T = 60^\circ\text{C}$).

size of foam is only $440\text{ }\mu\text{m}$, and the increase in KYPAM-6s concentration effectively hinders the diffusion behavior of gas molecules (the maximum size decreased). This hindering behavior is evident in the enhanced foam prepared by XG and DG. At the concentration of 0.75 g/L , the platform region appears at 10 min (particle size range $54\text{--}94\text{ }\mu\text{m}$) with a frequency of 17.91% . At 20 min , the platform region only expands to $80\text{--}140\text{ }\mu\text{m}$ with a frequency of 12.23% . At 30 min , two

platform regions appear in the curve (particle size range $81\text{--}170\text{ }\mu\text{m}$ and $230\text{--}277\text{ }\mu\text{m}$). Although the platform region also extends to a large particle size range in the later observation period, the maximum range is only extended to $260\text{--}290\text{ }\mu\text{m}$ ($t = 30\text{ min}$), and only a very few distribution frequencies (0.28%) are observed after $300\text{ }\mu\text{m}$. Therefore, the presence of DG effectively obstructs the diffusion behavior of gas molecules from small bubbles to large bubbles. In the later observation

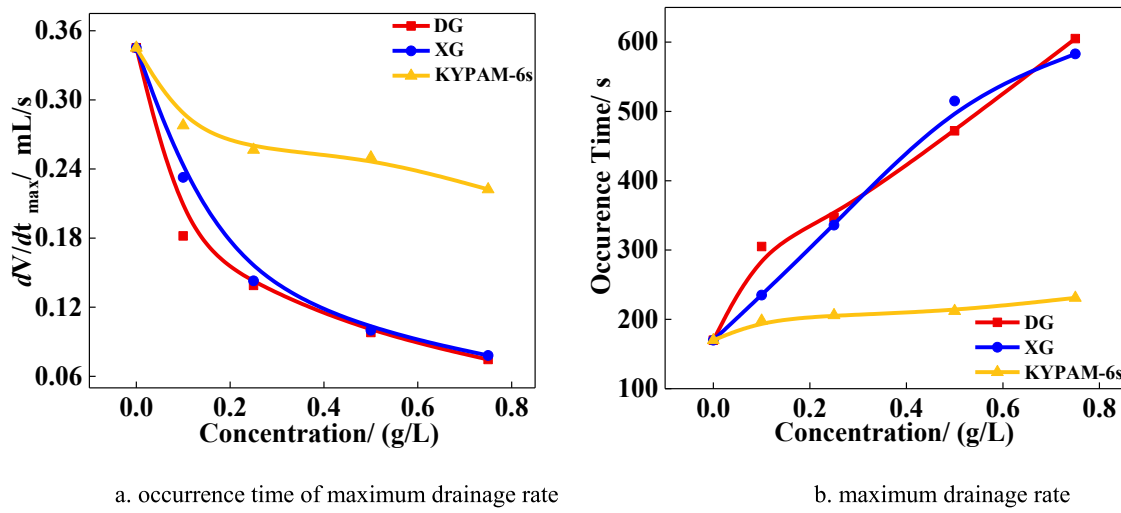


Fig. 21. Maximum drainage rate and its occurrence time of enhanced foam prepared by different polymers ($T = 60^\circ\text{C}$).

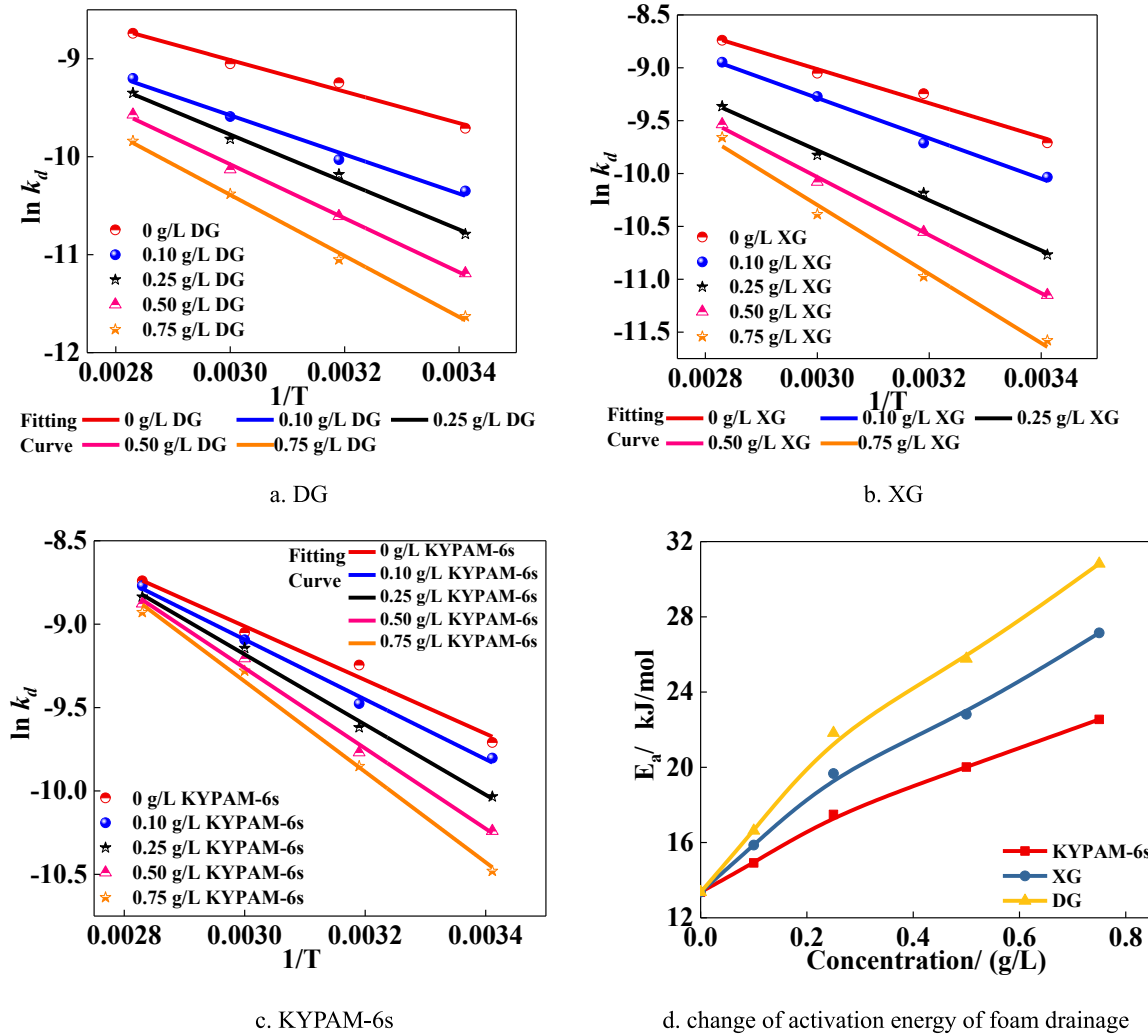


Fig. 22. Changes of Arrhenius fitting curves and activation energy of enhanced foam drainage in different polymers ($T = 60^\circ\text{C}$).

period, a large number of evenly distributed bubbles with small particle sizes ($<200 \mu\text{m}$) can still be observed within the field of vision.

The changes in the bubble number and the D_{ad} of the enhanced foam systems of different polymers during the decays were also analyzed. The

statistical results are shown in Fig. 24. The presence of polymers inhibits the bubble number from declining and the D_{ad} from increasing. During the experiment, the increase in the metal ion valence and salinity in the APG solution is conducive to improve the stability of the foam and

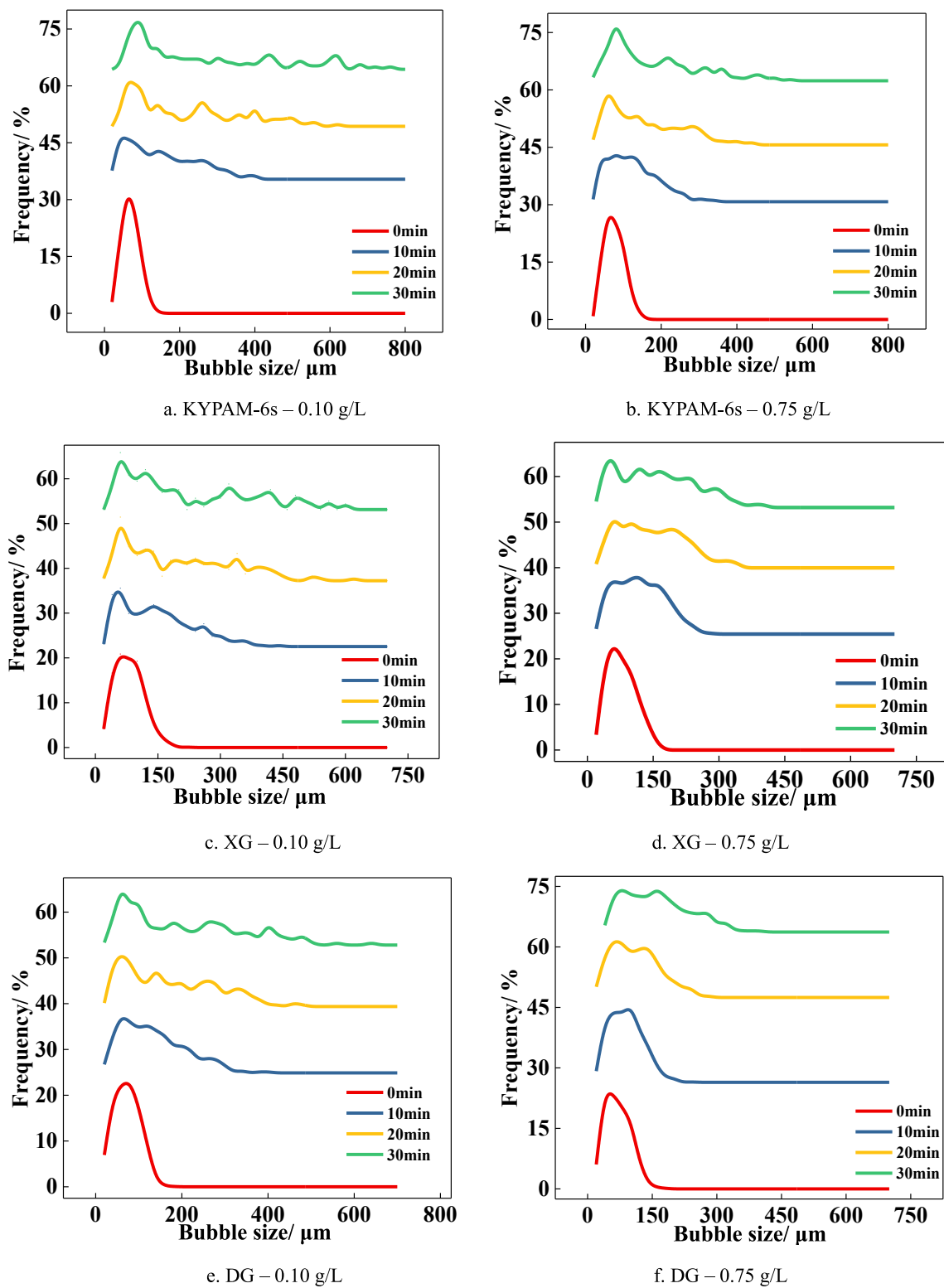


Fig. 23. The change of bubble size distribution during the decay of enhanced foam with different polymers ($T = 60^\circ\text{C}$).

inhibit the diffusion of gas molecules to large bubbles to a certain extent. However, this inhibition capability is lower than that of polymers, and a small increase of polymer concentration can significantly enhance this behavior. For KYPAM-6s with the weakest foam stabilization ability of the three polymers, when the concentration is 0.10 g/L, the D_{ad} increases from 68.84 μm (0 min) to 258.83 μm (30 min). When the concentration is increased to 0.25 g/L, the D_{ad} of the foam increases from

77.81 μm (0 min) to 223.81 μm (30 min), and the D_{ad} is significantly reduced. In terms of the inhibiting ability for the diffusion behavior of gas molecules, the order of strength is DG > XG > KYPAM-6s. The ability of DG to inhibit foam coarsening behavior is the most sensitive to concentration. When the DG concentration was only 0.10 g/L, from 0 min to 30 min, the bubble number decreases from 1314 to 187, and the D_{ad} increases from 72.30 μm to 201.90 μm . When the concentration

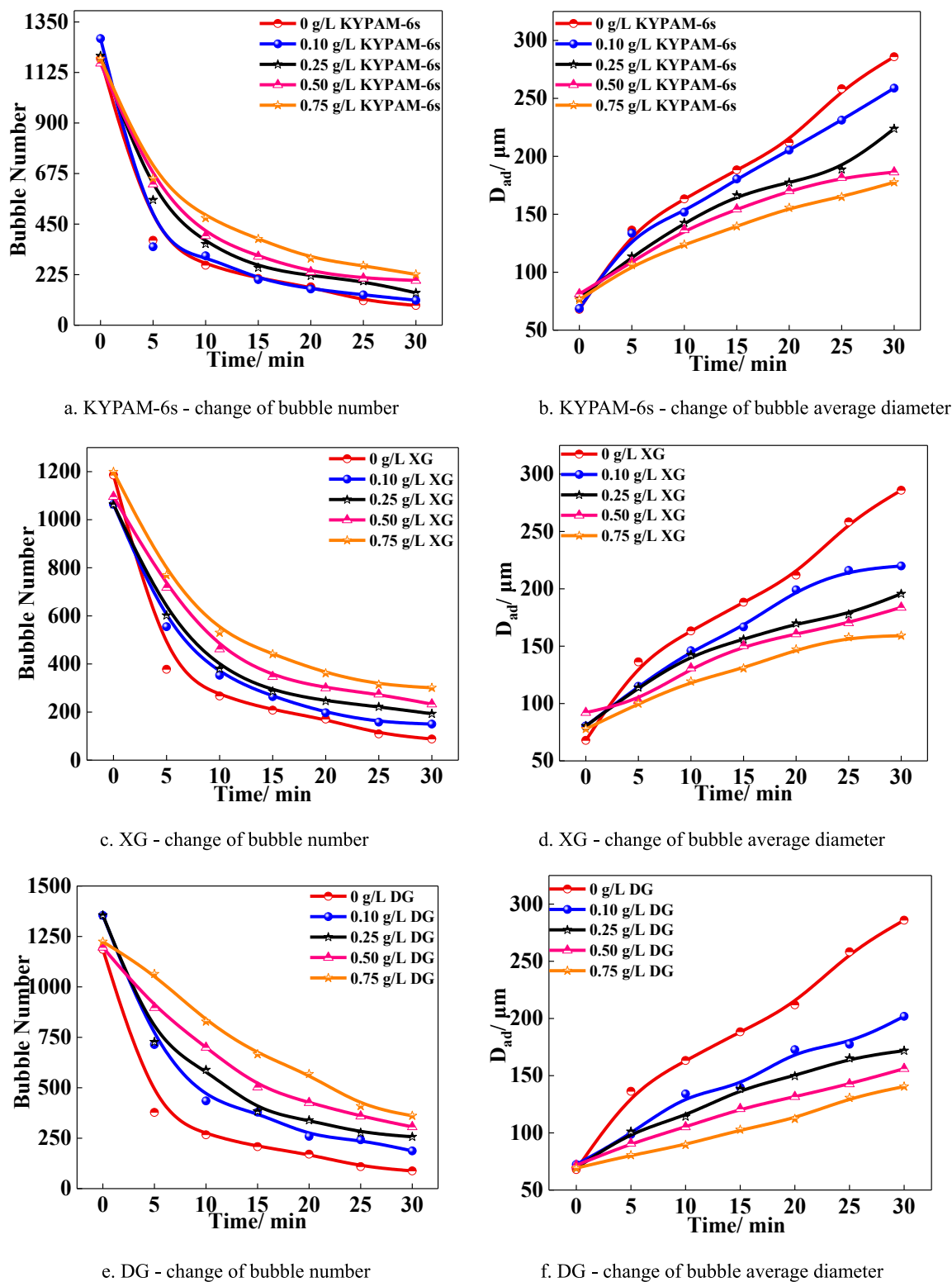


Fig. 24. Changes in bubble number and D_{ad} of bubbles during the decay of enhanced foam with different polymers ($T = 60^\circ\text{C}$).

increases to 0.25 g/L, the bubble number decreases from 1287 to 257, and the D_{ad} increases from 69.19 μm to 171.90 μm . The existence of DG greatly increases the stability of the foam system because DG and APG can form a strong liquid film and adsorption layer in the foam (a follow-up study in section 3.3.3), thus increasing the difficulties of gas molecules migration from small bubbles to large bubbles and reducing the mass transfer rate of gas molecules.

According to the D_{ad} change of enhanced foam prepared by different types of polymers, a scatter image of D_{ad}^3 -time (Fig. 25-a, b and c) was drawn and linearly fitted. The relationship between the slope of the line equation (i.e. Ostwald ripening rate) and the polymer concentration is shown in Fig. 25-d. With the increase in polymer concentration, the ripening rate of foam system decreases significantly. DG has the strongest ability to reduce the ripening rate of foam. At 100 g/L, the ripening

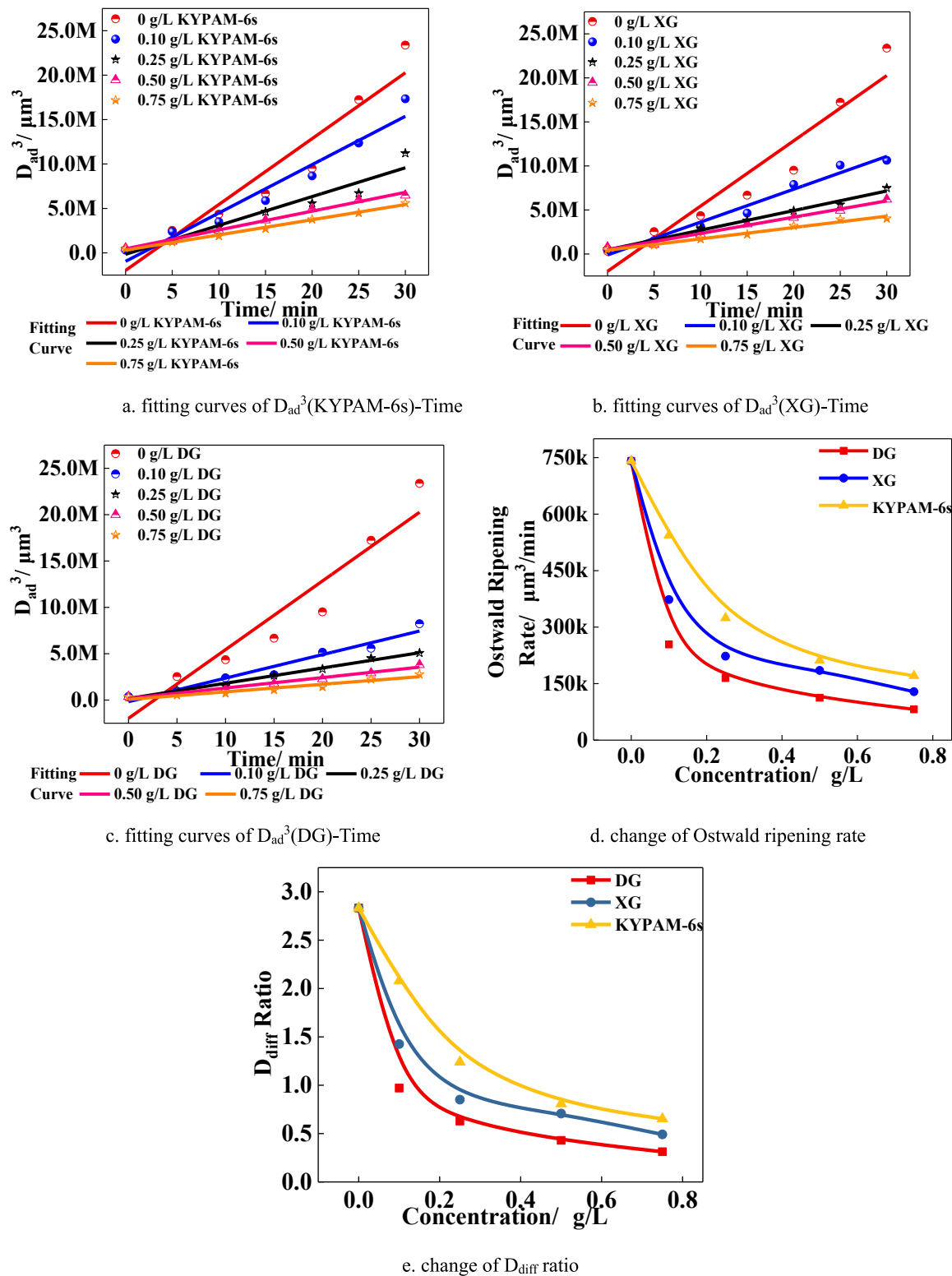


Fig. 25. Changes of Ostwald ripening rate and D_{diff} ratio during enhanced foam decay with different polymers.

rate of foam decreases from $7.41 \times 10^5 \mu\text{m}^3/\text{min}$ (blank group) to $2.54 \times 10^5 \mu\text{m}^3/\text{min}$. When the concentration of DG continues to increase, the ripening rate decreases linearly with the increase in concentration. However, when concentration increases to 0.75 g/L , the ripening rate decreases to $8.17 \times 10^4 \mu\text{m}^3/\text{min}$, which is an order of magnitude lower than that at 100 g/L . In addition, XG achieves satisfactory foam stabilization effect with the ripening rate of foam dropping to 1.29×10^5

$\mu\text{m}^3/\text{min}$ at the same concentration (0.75 g/L). The decrease in the ripening rate of the three polymers reflects a reduction in the gas mass transfer rate. Polymers can greatly reduce the mass transfer rate of gas molecules mainly because of the polymer molecules in the liquid film. Water molecules and polymer polar groups (such as hydroxyl, carboxyl, and amide groups), especially for the two biopolysaccharides DG and XG contain a large number of hydroxyl and carboxyl groups compared with

KYPAM-6s. The interaction between these groups and water molecules affects the solubility of water molecules on the solution surface and their diffusion ability in solution, enhance the water adsorption capability of the lamella and thereby reduce the mass transfer efficiency. In addition, the lamella formed by the interaction between polymer and surfactant has a large thickness, which increases the distance of gas molecule mass transfer and thus reduces the mass transfer coefficient of gas molecules. Fig. 25-e shows that the ability of polymers to reduce mass transfer efficiency of gas molecules is higher than that of inorganic salts. The D_{diff} ratio of KYPAM-6s at 0.75 g/L (0.65) is still lower than that of CaCl_2 at 100 g/L (0.87). Compared with the enhanced foam of KYPAM-6s, the enhanced foam of DG and XG has lower ripening rate (Fig. 25-d) and mass transfer rate of gas molecules. In summary, the polymer is more able to stabilize the foam than the inorganic salts.

The U_{poly} of different enhanced foam systems are shown in Fig. 26. For DG with the best foam stability, when the concentration is 0.10 g/L, the U_{poly} of the foam systems increases from 0.40 (0 min) to 0.65 (30 min) in the observation time. By contrast, the U_{poly} of XG enhanced foam increases from 0.42 to 0.69 under the same polymer concentration. Within a certain concentration range, XG has a lower ability to inhibit the diffusion of gas molecules from small bubble to large bubbles than DG, resulting in a higher degree of disproportionation of the size of the XG enhanced foam than that of DG ($U_{poly}(\text{XG}) > U_{poly}(\text{DG})$). When the concentration is 0.75 g/L, the U_{poly} of DG enhanced foam increases from 0.41 to 0.54, and the U_{poly} of XG enhanced foam increases from 0.41 to 0.55. With the increase of polymer concentration, the

disproportionation degree of XG and DG enhanced foams in size has been greatly reduced compared with that of low concentration polymers. In addition, the ability of DG and XG to hinder the mass transfer of gas molecules between bubbles is close when the polymer concentration is higher than a certain level. This conclusion confirms the data analysis in the previous article. According to Laplace equation, bubbles with similar curvature can slow down the mass transfer process between the foam film, indicating that when the U_{poly} of the foam system is small (i.e., the closer the bubble curvature), the PSD of the bubbles is uniform and highly favorable to reduce the mass transfer rate of gas molecules. Although U_{poly} could not directly reflect the changes in the geometric size of the foam system similar to PSD, D_{ad} and the bubble number, it can reflect the uniformity of the foam system. The uniformity of the foam system could slow down the foam coarsening to some extent.

3.3.3. Effect of polymer on the properties of APG aqueous solution

The apparent viscosity (η) of three polymers mixed with APG-10 was studied ($C_{\text{APG-10}} = 6 \text{ g/L}$, $T = 60^\circ\text{C}$, $\gamma = 7.34 \text{ s}^{-1}$). When natural gas foam prepared by the high-speed stirring method was used, the viscosity of the original solution cannot reflect the bulk viscosity of the foam system. Therefore, the Brookfield DV-III viscometer was adopted to measure the apparent viscosity (Fig. 27) of the solution after high-speed shearing (8000 r/min, shearing time 2 min, the stirring speed and time is consistent with that of foam preparation). DG has excellent thickening properties and shearing resistance. After a high-speed shear, the solution can still maintain a high bulk viscosity, and its viscosity retention can

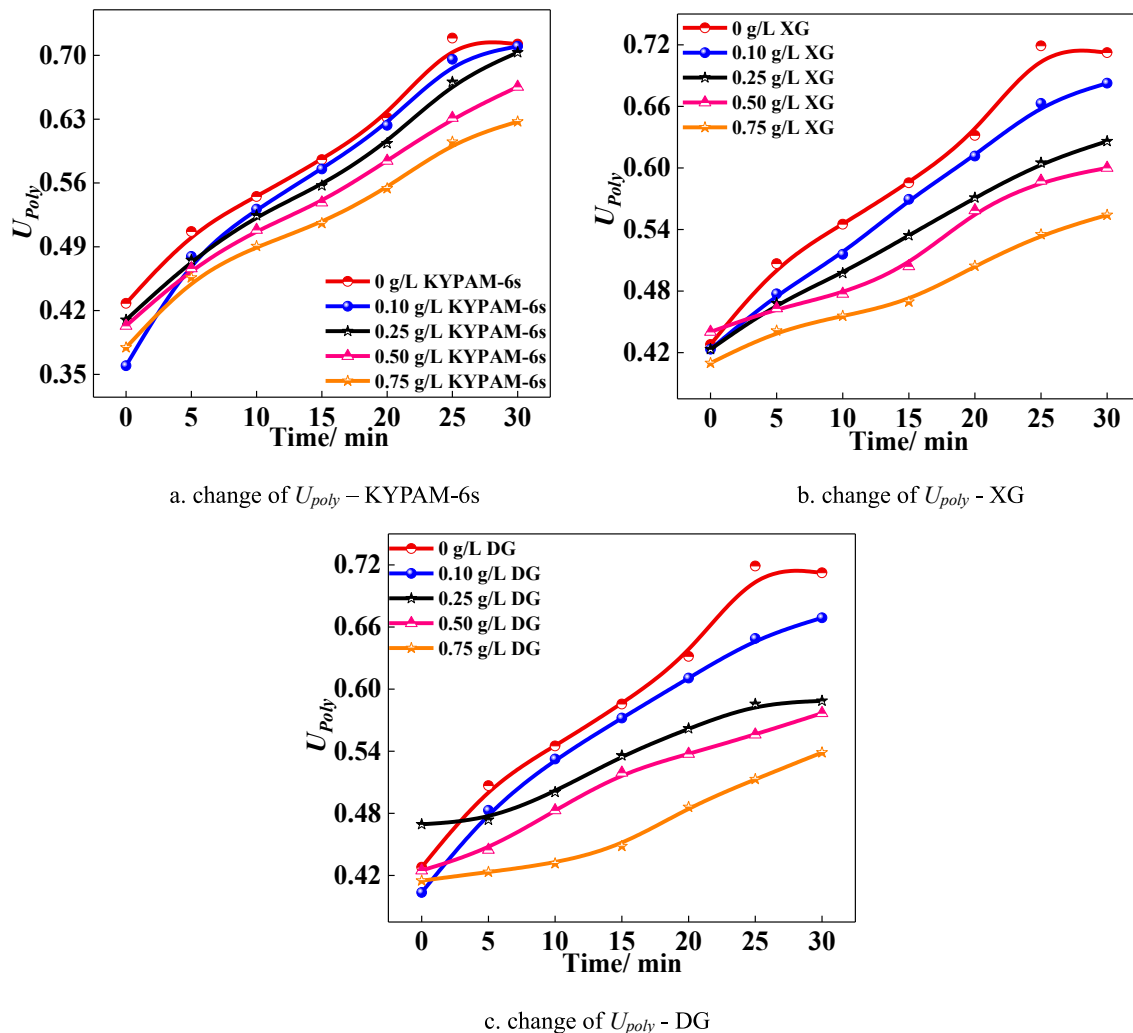
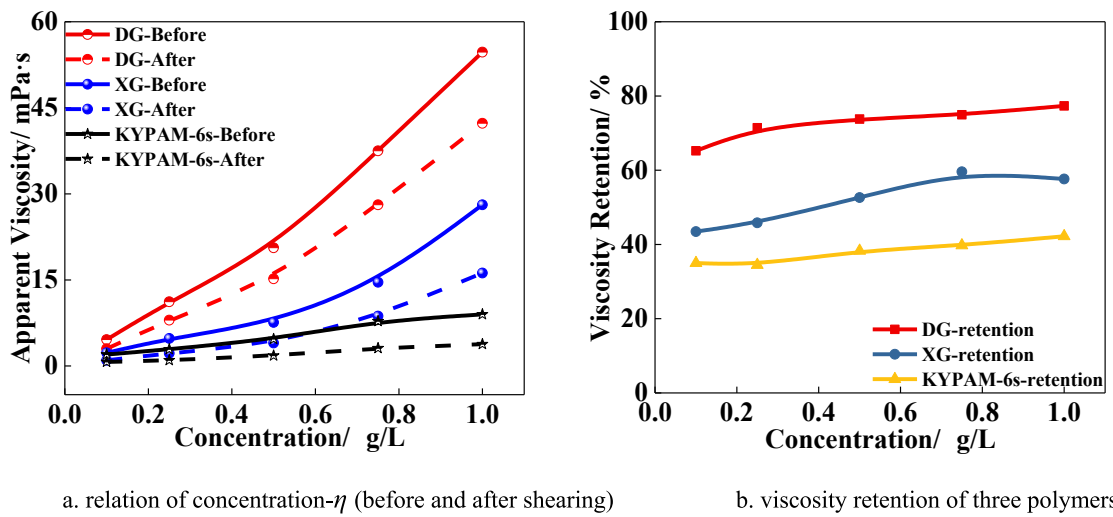


Fig. 26. Changes of U_{poly} during enhanced foam decay with different polymers.

a. relation of concentration- η (before and after shearing)

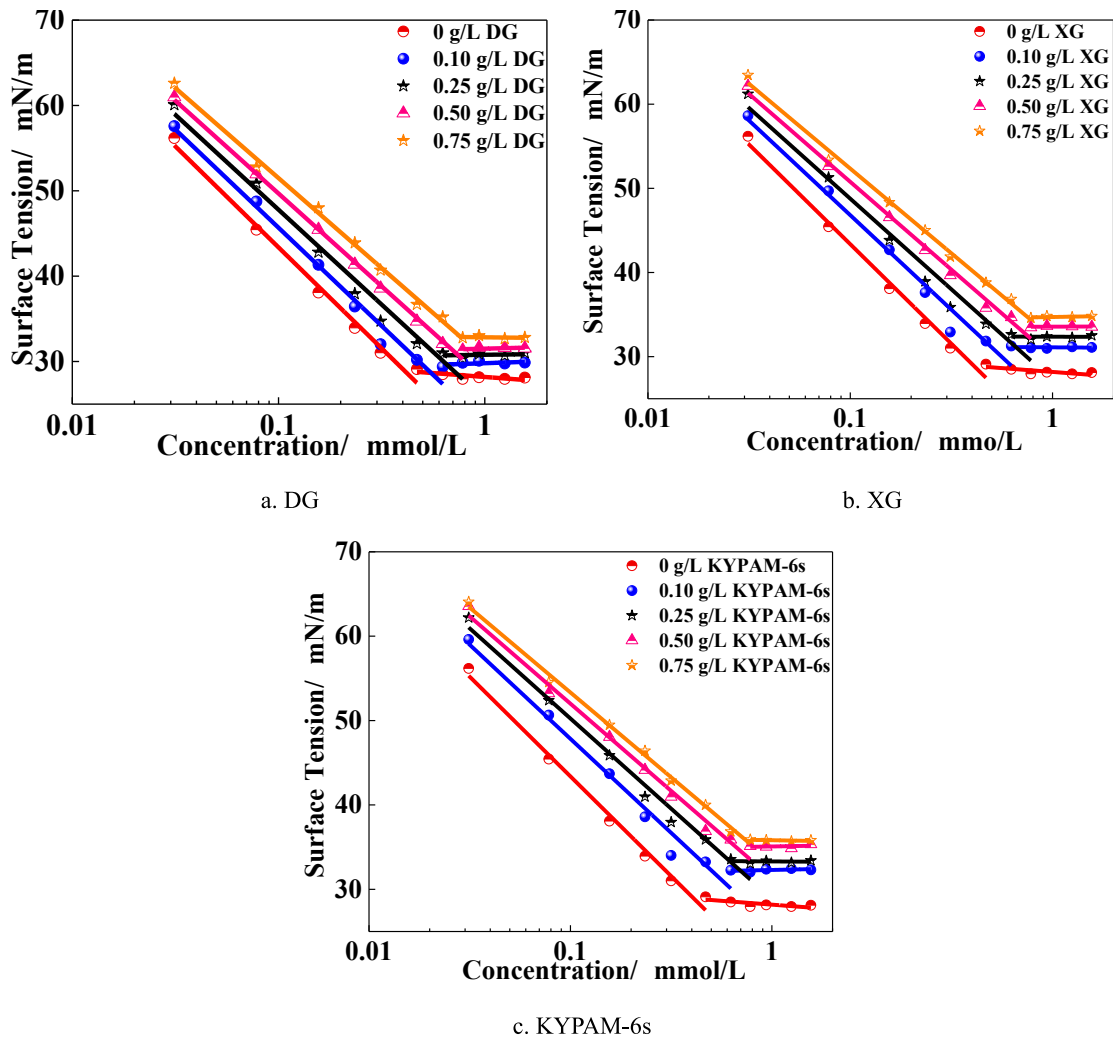
b. viscosity retention of three polymers

Fig. 27. The relation of concentration- η (a) and concentration-viscosity retention (a) ($T = 60^\circ\text{C}$, $\gamma = 7.34 \text{ s}^{-1}$).

reach 65.22%–77.33%. For KYPAM-6s, the apparent viscosity of the solution cannot reach higher than 10 mPa s in the test concentration range before shearing ($\eta_1 \text{ g/L} = 9.2 \text{ mPa s}$). The shearing resistance of the solution is poor, and the viscosity retention after shear is only 35–42.22%. The apparent viscosity of the solution is large and thus

increases the strength of the liquid film. In addition, the larger apparent viscosity weakens the fluid flow of the lamella and makes it difficult for the liquid to be drained. The rate of thinning process of the lamella and enhances the foam system stability.

The surface adsorption properties of the foam systems of the three

Fig. 28. Change of surface tension of APG-10 solution with different polymers (gas phase is natural gas, $T = 60^\circ\text{C}$).

polymers were also studied. The concentration of APG-10 was the same as that in section 3.1.2. The concentrations of the three polymers were 0.10, 0.25, 0.50, and 0.75 g/L. The influence of different concentrations of polymers on the surface tension of APG-10 is shown in Fig. 28. The *cmc* of APG-10 under different conditions can be calculated by linear fitting the scatter points before and after the surface tension balance was reached. Similarly, the surface pressure and minimum adsorption surface area of APG-10 solution after adding different types of polymers were calculated using to equations (11) and (12), and the results are shown in Fig. 29.

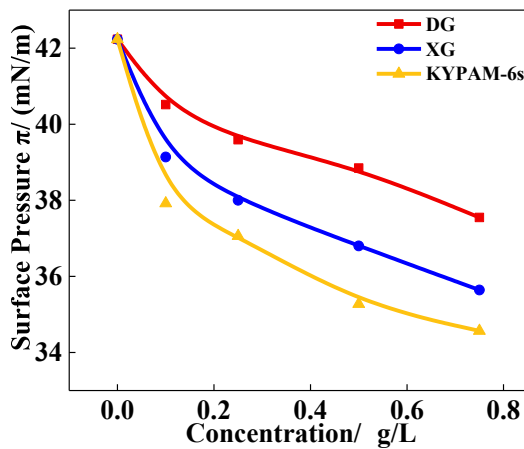
Fig. 28 shows that *cmc* and equilibrium surface tension increase after polymer addition because the latter has a certain adverse effect on the adsorption of APG molecules on the surface. The selected polymer contains a large number of hydrophilic groups. After interacting with APG to form a compound, the adsorption area formed by the compound on the gas–liquid interface is higher than the surface area occupied by a single surfactant molecule (Deo and Somasundaran, 2005). Fig. 29 shows that with the increase in polymer concentration, the adsorption area formed by the compound at the gas–liquid interface continues to increase. Moreover, with the increase in bulk viscosity, the mass transfer rate of APG-10 from the bulk to the surface decreases to a certain extent. The combined effect of the two causes that the APG distribution on the gas–liquid interface is relatively sparse. Therefore, due to the interaction between the polymer and APG-10, the foaming property of APG-10 solution is weakened, whereas the foam system gains stability. On the basis of the change of surface pressure (Fig. 29-a), the surface pressure increases to a certain extent after polymer addition, and the order of the increase in surface pressure is KYPAM-6s < XG < DG. According to the Laplace equation, the order of capillary pressure of enhanced foam during foam decay is KYPAM-6s > XG > DG. This finding confirms the changes in the rate of drainage and coarsening of the enhanced foam with different polymers and also corresponds to the drainage half-life of the foam system.

In order to further illustrate the influence of the three polymers on the structural strength of the foam lamella, the ESEM was used to observe the micromorphology of three enhanced foam solutions, the aqueous solution micromorphology of three enhanced foam systems are shown in Fig. 30. The micelle structure of APG-10 is not observed in the micromorphology of the three enhanced foam system, but the structure of three solutions is quite different. The micromorphology of KYPAM-6s enhanced foam systems presents a network structure, but the grid size in the spatial network is large, the average size of the network cavity is about 42.15 μm. Moreover, part of the network skeleton presents a filamentous structure, and this morphology reduces the overall structure

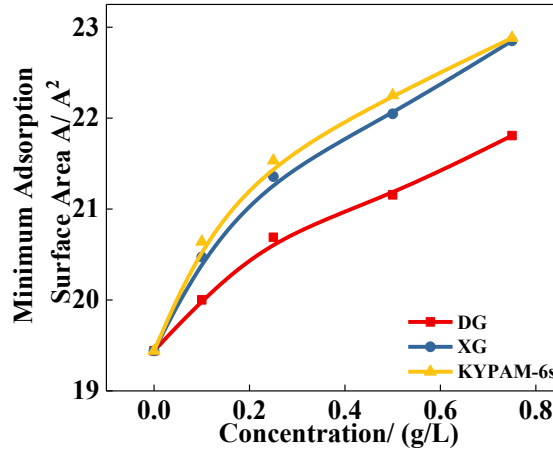
strength, which further decreases the structure of the foam lamella accordingly. XG enhanced foam system also has a network structure, with stronger strength than KYPAM-6s, and it presents a sponge multi-layer structure as a whole, making the lamella possess a certain degree of flexibility, such structure makes the lamella difficult to rupture when it deforms through the narrow throat. The DG enhanced foam also presents a multi-layer structure, but unlike the other two, the DG system has membranes structure. The existence of the membrane structure not only further enhances the multi-layer structure, but also hinders the mass transfer of gas molecules inside the bubble to the outside, and enhances the trapping effect of the lamella on the internal gas, this is also the main reason why the stability of the DG enhanced foam is the strongest of the three. The micromorphology of the three enhanced foam systems have been mutually confirmed.

4. Conclusions

- (1) A mathematical model of foam drainage was established on the basis of the relationship between drainage volume and time of foam under different conditions. The relationship between the drainage rate and time of foam and the k_d of foam under different conditions were obtained by differentiating the model. A good linear relationship was found between $\ln k_d$ and T^{-1} , which conforms to the Arrhenius equation. According to the fitting results, E_a of the foam drainage under different conditions was obtained. The drainage process of the foam from the perspective of kinetics can be analyzed by comparing the maximum drainage rate and its occurrence time, k_d , E_a and other indicators.
- (2) Geometric information such as bubble number, diameter distribution frequency, and D_{ad} of the foam decay process under different conditions were studied by using statistical methods. The Ostwald ripening rate and gas molecular diffusion constant can quantitatively analyze the kinetics of foam decay.
- (3) Alkyl chain length affects the stability of APG foam: the increase in alkyl chain length within a certain range (8 → 10.9) is conducive to prolonging the drainage time of foam, reducing the mass transfer rate of gas molecules between lamella, and thereby decreasing the Ostwald ripening rate of bubbles. The length of alkyl chain continued to increase (10.9 → 12), and the stability of the foam system declined. Analysis of the surface properties of surfactants revealed that within a certain range, when the APG alkyl chain length was long, the adsorption capability was strengthened, and the minimum adsorption surface area was lowered, which is conducive to the formation of a tight surfactant



a. change of surface pressure



b. change of minimum adsorption surface area

Fig. 29. Change of surface adsorption of APG-10 solution with different polymers.

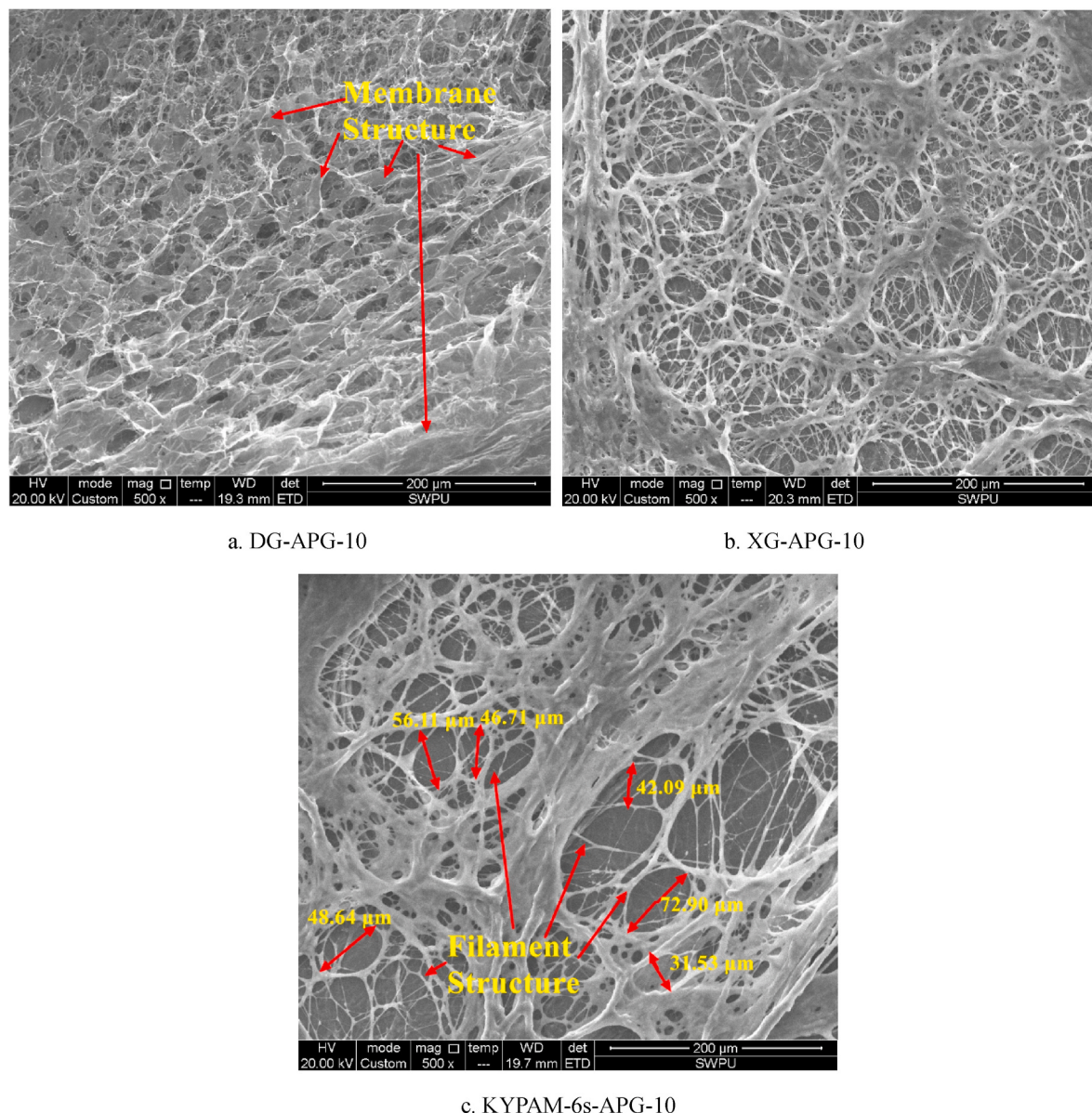


Fig. 30. The aqueous solution micromorphology of different enhanced foam system.

- molecular layer. However, with the continuous growth of APG alkyl chain length, the occupied area of APG molecules on the gas–liquid interface increased and the number of APG molecules on the gas–liquid interface was reduced.
- (4) Increasing the salinity and metal ions is beneficial to the stability of the foam. Analysis of the surface properties of different metal ions at different salinities revealed that with the increase in salinity and metal ions valence, APG molecules can form a dense and ordered molecular layer on the gas–liquid interface, thereby generating a stronger surface adsorption layer, delayed the drainage of the natural gas foam system and enhancing its stability.

- (5) Compared with inorganic salts, the polymer can significantly enhance the stability of APG, and the ability of three polymers to stabilize the foam in the order of DG > XG > KYPAM-6s. The reasons for the polymer stabilizing the APG foam are as follows:
- a. The polymer significantly increased the bulk viscosity of the APG solution. The larger apparent viscosity weakened the fluidity of the lamella and delayed the thinning process.

b. The order of surface tension of the enhanced foam was APG-DG < APG-XG < APG-KYPAM-6s. In terms of Laplace equation, the order of capillary pressure of enhanced foam during the drainage and bubble coarsening was the same as that of surface tension. This result confirms the changes in the rate of drainage and coarsening of the enhanced foam of APG with different polymers.

c. The membrane in the DG enhanced foam system not only reduces the gas permeability through the lamella and slows the gas diffusion rate, but also enhances the lamella elasticity together with its multi-layer sponge structure, improved foam stability to a certain extent.

Credit author statement

Conceptualization: Nanjun Lai, Yiping Wen; Methodology: Nanjun Lai, Yiping Wen; Investigation: Yiping Wen, Zhiling Song; Resources: Nanjun Lai, Wenhong Li, Yongqiang Zhang, Zhaofeng Du and Lijuan Han; Data Processing: Yiping Wen, Zhiling Song; Writing-original draft preparation: Yiping Wen, Zhiling Song; Writing-review and editing:

Yiping Wen; Supervision: Nanjun Lai.

Declaration of competing interest

The authors declare that they have no known competing financial interests or personal relationships that could have appeared to influence the work reported in this paper.

Acknowledgement

We gratefully acknowledge financial support from the Open Fund (2019DE0101) of State Engineering Laboratory of Low-permeability Oil & Gas Reservoir Exploration, the National Natural Science Foundation of China (51674210).

Appendix A. Supplementary data

Supplementary data to this article can be found online at <https://doi.org/10.1016/j.petrol.2020.108039>.

References

- Calder, I.R., Neal, C., 1983. Evaporation from saline lakes: a combination equation approach. *Hydrog. Sci. J.* 29 (1), 89–97.
- Chang, S., Grigg, R.B., 1998. Effects of foam quality and flow rate on CO₂-foam behavior at reservoir conditions. In: SPE/DOE Symposium on Improved Oil Recovery. Tulsa, Oklahoma, USA, SPE Paper 39679.
- Deo, P., Somasundaran, P., 2005. Interactions of hydrophobically modified polyelectrolytes with nonionic surfactants. *Langmuir* 21 (9), 3950–3956.
- Dong, X., Liu, H., Sun, P., et al., 2012. Air-foam-injection process: an improved-oil-recovery technique for waterflooded lighted-oil reservoirs. *SPE Reservoir Eval. Eng.* 15 (4), 436–444.
- Du, D., Wang, D., Jia, N., et al., 2016. Experiments on CO₂ foam seepage characteristics in porous media. *Petrol. Explor. Dev.* 43, 499–505.
- Eastoe, J., Dalton, J.S., 2000. Dynamic surface tension and adsorption mechanisms of surfactants at the air-water interface. *Adv. Colloid Interface Sci.* 85 (2–3), 103–144.
- Farajzadeh, R., Krastev, R., Zitha, P.L.J., 2007. Foam film permeability: theory and experiment. *Adv. Colloid Interface Sci.* 137 (1), 27–44.
- Garrett, P.R., Wicks, S.P., Fowles, E., 2006. The effect of high volume fractions of latex particles on foaming and antifoam action in surfactant solutions. *Colloid. Surface. Physicochem. Eng. Aspect.* 282–283, 307–328.
- Hurtado, Y., Franco, C.A., Riazi, M., et al., 2020. Improving the stability of nitrogen foams using silica nanoparticles coated with polyethylene glycol. *J. Mol. Liq.* 300, 112256.
- Iglauer, S., Wu, Y., Shuler, P., et al., 2009. Alkyl polyglycoside surfactant-alcohol cosolvent formulations for improved oil recovery. *Colloid. Surface. Physicochem. Eng. Aspect.* 339, 48–59.
- Jacobi, W.M., Woodcock, K.E., Grove, C.S., 1956. Theoretical investigation of foam drainage. *Ind. Eng. Chem.* 48 (11), 2046–2051.
- Jhan, Y., Tsay, R., 2014. Salt effects on the hydration behavior of zwitterionic poly (sulfobetain methacrylate) aqueous solutions. *J. Taiwan Inst. Chem. Eng.* 45 (6), 3139–3145.
- Kam, S.I., Frenier, W.W., Davies, S.N., et al., 2007. Experimental study of high-temperature foam for acid diversion. *J. Petrol. Sci. Eng.* 58 (1–2), 138–160.
- Kovsek, A.R., Bertin, H.J., 2002. Estimation of foam mobility in heterogeneous porous media. In: SPE/DOE Symposium on Improved Oil Recovery. Tulsa, Oklahoma, USA, SPE Paper 75181.
- Kuru, E., Okunsebor, O.M., Li, Y., 2005. Hydraulic optimization of foam drilling for maximum drilling rate in vertical wells. *SPE Drill. Complet.* 20 (4), 258–267.
- Lang, L., Li, L., Wang, X., et al., 2019. Experimental study and field demonstration of air-foam flooding for heavy oil EOR. *J. Petrol. Sci. Eng.* 185, 106659.
- Liang, S., Hu, S., Li, J., et al., 2019. Study on EOR method in offshore oilfield: combination of polymer microspheres flooding and nitrogen foam flooding. *J. Petrol. Sci. Eng.* 178, 629–639.
- Lioumbas, J.S., Georgiou, E., Kostoglou, M., et al., 2015. Foam free drainage and bubbles size for surfactant concentrations below CMC. *Colloid. Surface. Physicochem. Eng. Aspect.* 487, 92–103.
- Liu, Y., Grigg, R., Svec, R.K., 2006. Foam mobility and adsorption in carbonate core. In: SPE/DOE Symposium on Improved Oil Recovery. Tulsa, Oklahoma, USA, SPE Paper 99756.
- Nguyen, Q.P., Currie, P.K., Zitha, P.L.J., 2005. Effect of crossflow on foam-induced diversion in layered formations. *SPE J.* 10 (1), 54–65.
- Pang, Z., Liu, H., Zhu, L., 2015. A laboratory study of enhancing heavy oil recovery with steam flooding by adding nitrogen foams. *J. Petrol. Sci. Eng.* 128, 184–193.
- Parlar, M., Parris, M.D., Jasinski, R.J., et al., 1995. An experimental study of foam flow through Berea sandstone with applications to foam diversion in matrix acidizing. In: SPE Western Regional Meeting. Bakersfield, California, USA. SPE Paper 29678.
- Paulson, O., Pugh, R.J., 1996. Flootation of inherently hydrophobic particles in aqueous solutions of inorganic electrolytes. *Langmuir* 12 (20), 4808–4813.
- Pei, H., Zhang, G., Ge, J., et al., 2010. Investigation of Polymer-Enhanced Foam Flooding with Low Gas/liquid Ratio for Improving Heavy Oil Recovery, Canadian Unconventional Resources and International Petroleum Conference. Calgary, Alberta, Canada, SPE Paper 137171.
- Rafati, R., Hamidi, H., Idris, A.K., et al., 2012. Application of sustainable foaming agents to control the mobility of carbon dioxide in enhanced oil recovery. *Egypt. J. Petrol.* 21, 155–163.
- Rossen, W.R., Wang, M., 1999. Modeling foams for acid diversion. *SPE J.* 4 (2), 92–100.
- Salman, M., Kostarellos, K., Sharma, P., et al., 2019. Application of Miscible Ethane Foam for Gas EOR Conformance in Low Permeability Heterogeneous Harsh Environments. Unconventional Resources Technology Conference, Denver, Colorado, USA.
- Save, S.V., Pangarkar, V.G., 1994. Characterisation of colloidal gas aaphrons. *Chem. Eng. Commun.* 127 (1), 35–54.
- Schmitt, V., Cattelet, C., Leal-Calderon, F., 2004. Coarsening of alkane-in-water emulsions stabilized by nonionic poly (oxyethylene) surfactants: the role of molecular permeation and coalescence. *Langmuir* 20, 46–52.
- Stewart, P.S., Davis, S.H., Hilgenfeldt, S., 2015. Microstructural effects in aqueous foam fracture. *J. Fluid Mech.* 785, 425–461.
- Stubenrauch, C., Hamann, M., Preisig, N., et al., 2017. On how hydrogen bonds affect foam stability. *Adv. Colloid Interface Sci.* 247, 435–443.
- Sun, L., Wei, P., Pu, W., et al., 2016. The oil recovery enhancement by nitrogen foam in high-temperature and high-salinity environments. *J. Petrol. Sci. Eng.* 147, 485–494.
- Vassenden, F., Holt, T., 1998. Experimental foundation for relative permeability modeling of foam. In: SPE/DOE Symposium on Improved Oil Recovery. Tulsa, Oklahoma, USA, SPE Paper 39660.
- Verga, I., Meszaros, R., Stubenrauch, C., et al., 2012. Adsorption of sugar surfactants at the air/water interface. *J. Colloid Interface Sci.* 379 (1), 78–83.
- Wang, J., Nguyen, A.V., Farrokhpour, S., 2016. A critical review of the growth, drainage and collapse of foams. *Adv. Colloid Interface Sci.* 228, 55–70.
- Wang, F., Li, Z., Chen, H., et al., 2017. Fractal characterization of dynamic structure of foam transport in porous media. *J. Mol. Liq.* 241, 675–683.
- Weaire, D., 2008. The rheology of foam. *Curr. Opin. Colloid Interface Sci.* 13 (3), 171–176.
- Wei, P., Li, J., Xie, Y., et al., 2020. Alkyl polyglucosides for potential application in oil recovery process: adsorption behavior in sandstones under high temperature and salinity. *J. Petrol. Sci. Eng.* 189, 107057.
- Xu, X., Saeedi, A., Rezaee, R., et al., 2015. Investigation on a novel polymer with surface activity for polymer enhanced CO₂ foam flooding. In: SPE International Symposium on Oilfield Chemistry. The Woodlands, Texas, USA. SPE Paper 173716.
- Xu, X., Saeedi, A., Liu, K., 2016. Bulk phase behavior and displacement performance of CO₂ foam induced by a combined foaming formulation. *J. Petrol. Sci. Eng.* 147, 864–872.
- Xu, X., Saeedi, A., Liu, K., 2017. An experimental study of combined foam/surfactant polymer (SP) flooding for carbon dioxide-enhanced oil recovery (CO₂-EOR). *J. Petrol. Sci. Eng.* 149, 603–611.
- Wei, P., Pu, W., Sun, L., et al., 2018. Alkyl polyglycosides stabilized foam for gas controlling in high-temperature and high-salinity environments. *J. Ind. Eng. Chem.* 60, 143–150.
- Xu, L., Rad, M.D., Telmadarrie, A., et al., 2018. Synergy of surface-treated nanoparticle and anionic-nonionic surfactant on stabilization of natural gas foams. *Colloids Surf., A* 550, 176–185.
- Yan, Y., Zhang, N., Qu, C., et al., 2005. Investigation of the kinetics of liquid drainage from colloidal gas aaphrons. *Acta Chimica Sinica* 63 (18), 1686–1692.
- Yang, J., Wang, X., Peng, X., et al., 2019. Experimental studies on CO₂ foam performance in the tight cores. *J. Petrol. Sci. Eng.* 175, 1136–1149.
- Yin, D., Zhang, X., 2013. Evaluation and research on performance of a blend surfactant system of alkyl polyglycoside in carbonate reservoir. *J. Petrol. Sci. Eng.* 111, 153–158.
- Zana, R., 2002. Dimeric and oligomeric surfactants, behavior at interfaces and in aqueous solution: a review. *Adv. Colloid Interface Sci.* 97 (1–3), 205–253.
- Zhang, K., Li, S., Liu, L., 2020. Optimized foam-assisted CO₂ enhanced oil recovery technology in tight oil reservoirs. *Fuel* 267, 117099.
- Zhu, J., Yang, Z., Li, X., et al., 2019a. Setting behavior of the proppants in viscoelastic foams on the bubble scale. *J. Petrol. Sci. Eng.* 181, 106216.
- Zhu, J., Yang, Z., Li, X., et al., 2019b. Experimental study on the microscopic characteristics of foams stabilized by viscoelastic surfactant and nanoparticles. *Colloids Surf., A* 572, 88–96.